Title:

Proximate Kitaev Quantum Spin Liquid Behavior in a Honeycomb Magnet

Authors:

A. Banerjee, C.A. Bridges, J-Q. Yan, A.A. Aczel, L. Li, M.B. Stone, G.E. Granroth, M.D. Lumsden, Y. Yiu, J. Knolle, S. Bhattacharjee, D.L. Kovrizhin, R. Moessner, D.A. Tennant, D.G. Mandrus, S.E. Nagler

Introduction:

Quantum spin liquids (QSLs) are topological states of matter exhibiting remarkable properties such as the capacity to protect quantum information from decoherence. While their featureless ground states have precluded their straightforward experimental identification, excited states are more revealing and particularly interesting due to the emergence of fundamentally new excitations such as Majorana Fermions. Ideal probes of these excitations are inelastic neutron scattering experiments. These we report here for a ruthenium-based material, α-RuCl$_3$, continuing a major search (so far concentrated on iridium materials inimical to neutron probes) for realizations of the celebrated Kitaev honeycomb topological QSL. Our measurements confirm the requisite strong spin-orbit

1 **coupling and low-temperature magnetic order matching predictions proximate to the QSL.**

2 **We find stacking faults, inherent to the highly two-dimensional nature of the material,**

3 **resolve an outstanding puzzle. Crucially, dynamical response measurements above**

4 **interlayer energy scales are naturally accounted for in terms of deconfinement physics**

5 **expected for QSLs. Comparing these with recent dynamical calculations involving gauge**

6 **flux excitations and Majorana fermions of the pure Kitaev model, we propose the**

7 **excitation spectrum of α-RuCl₃ as a prime candidate for fractionalized Kitaev physics.**

8

9 **Main Text:**

10

11 Exotic physics associated with frustrated quantum magnets is an enduring theme in condensed

12 matter research. The formation of quantum spin liquids (QSL) in such systems can give rise to

13 topological states of matter with fractional excitations[1,2,3,4]. Fractionalization describes the

14 counterintuitive phenomenon where an electron breaks apart into well-defined independent

15 quasiparticles. The realization of this physics in real materials is an exciting prospect that may

16 provide a path to a robust quantum computing technology[5]. Fractional excitations in the form of

17 pairs of S=1/2 spinons are observed in quasi-one-dimensional (1D) materials containing S=1/2

18 Heisenberg antiferromagnetic chains[6]. Recent evidence for the 2D QSL state, in the form of

19 possible spinon excitations, has been found in quantum antiferromagnets on triangular[3] and

20 Kagome[7] lattices. The exactly solvable Kitaev model on the honeycomb lattice[8] represents a

21 class of 2D QSL that supports two different emergent fractionalized excitations: Majorana

22 fermions and gauge fluxes[9,10]. The comparatively simple gauge flux can be visualized as a spin-

2

orbit coupled version of a plaquette observable like a resonance energy. The Majorana

Fermions, in general, do not have a straightforward real-space representation since they are not

associated with any real-space spin or charge density. An idea of their nature can be gleaned in

the strongly anisotropic limit of weakly coupled Ising dimers, where they can be thought of as

excitations taking the form of misaligned nearest-neighbor spin pairs on top of a ground state

consisting of a coherent superposition of satisfied dimers. How to observe such ephemeral

entities is one of the central challenges of condensed matter and materials physics today. It has

turned out that the signature of the Majorana fermion in the response function measured via

inelastic neutron scattering is perhaps one of the most direct ways of pinning down the

excitation's existence[10]. This manuscript reports precisely such a measurement.

The Kitaev model consists of a set of spin-1/2 moments $\{\vec{S}_i\}$ arrayed on a honeycomb lattice.

The Kitaev couplings, of strength K in eqn. (1) are highly anisotropic with a different spin

component interacting for each of the three bonds of the honeycomb lattice. In actual materials a

Heisenberg interaction (J) is also generally expected to be present, giving rise to the Heisenberg-

Kitaev (H-K) Hamiltonian[11,12].

$$\mathcal{H} = \sum_{i,j}\left(KS_i^m S_j^m + J\vec{S}_i.\vec{S}_j\right) \qquad \text{eqn. (1)}$$

where m is the component of the spin directed along the bond connecting spins (i,j). The QSL

phase of the pure Kitaev model (J=0), for both ferromagnetic and antiferromagnetic K, is stable

for weak Heisenberg perturbations.

1 Remarkably the Hamiltonian (1) has been proposed to accurately describe edge-shared

2 octahedrally-coordinated magnetic systems, shown in Fig. 1a, with dominant spin-orbit

3 coupling[11,12]. The focus to date has centered largely on Ir^{4+} compounds[13-19], however attempts to

4 measure the dynamical response[15] via inelastic neutron scattering (INS) have met with limited

5 success, due to the unfavorable magnetic form factor and strong absorption cross-section of the

6 Ir ions. Resonant inelastic x-ray scattering (RIXS) has provided important information

7 concerning higher energy excitations in the iridates[18] but cannot provide the meV energy

8 resolution necessary to provide a robust experimental signature of collective fractional

9 excitations that are expected to occur at energy scales of order $1 - 10$ meV[15].

10 An alternative approach is to explore materials with Ru^{3+} ions[20]. The realization that the material

11 α-$RuCl_3$[20-22] also has the requisite honeycomb lattice and strong spin-orbit coupling has

12 stimulated a groundswell of recent investigations[23-29]. Whilst these studies lend support to the

13 material as a potential Kitaev material, conflicting results centering on the low temperature

14 magnetic properties have hindered progress. To resolve this, we undertake a comprehensive

15 evaluation of the magnetic and spin-orbit properties of α-$RuCl_3$, and further measure the

16 dynamical response establishing this material as proximate to the widely searched for QSL.

17 We begin by investigating the crystal and magnetic structure of α-$RuCl_3$. The layered structure

18 of the material is shown in Fig. 1a. Figures 1b,c show the ABCABC stacking arrangement of the

19 layers expected in the trigonal structure (space group $P3_112$). That the layers are weakly bonded

20 to each other, similar to graphite, is demonstrated by the lattice specific heat (shown for a

21 powder in Fig. 1d). This displays a tell-tale T^2 behavior characteristic of highly 2D bonded

1   systems[30] rather than the usual T^3 observed in conventional 3D solids. Since the 2D layers are

2   weakly coupled the inter-layer magnetic exchanges will also be rather weak. In addition,

3   stacking faults are formed easily and significant regions of the sample can crystallize in

4   alternative stacking structures, for example ABAB[25] (See Supplementary Fig. 2).

5

6   Neutron diffraction shows low temperature magnetic order. The temperature dependence of the

7   strongest magnetic powder peak, with $T_N \approx 14$ K, is shown in Fig. 1e. Figure 1f shows the

8   temperature dependence of magnetic peaks in one 22.5 mg single-crystal, revealing two ordered

9   phases. The first, which orders below $T_N \approx 14$ K, is characterized by a wave-vector of $\mathbf{q_1} = (1/2$

10     $0\ 3/2)$ (indexed according to the trigonal structure), whilst the other phase ($\mathbf{q_2} = (1/2, 0\ 1)$) orders

11   below 8 K (See also Supplementary Fig.3).   These temperatures correspond precisely to

12   anomalies observed in the specific heat and magnetic susceptibility[25,26,29] (Supplementary Fig.

13   1). This is readily explained as the observed $L = 3/2$ phase corresponds naturally to a stacking

14   order of ABAB type along the c-axis, and the $L = 1$ corresponds to ABCABC stacking. Indeed,

15   the difference in 3D transitions is a residual effect of different interlayer bonding influencing the

16   ordering. Further, a comparison of intensities at $(1/2\ 0\ L)$ with $(3/2\ 0\ L)$[16] shows both phases

17   share identical zig-zag (ZZ) spin ordering in the honeycomb layers; a phase of the H-K model

18   adjacent to the spin liquid[11] (See Supplementary Table 1). By calibrating to structural Bragg

19   peaks the ordered moments are measured to be exceptionally low, with an upper bound of $\mu = 0.4$

20     $\pm\ 0.1\ \mu_B$. This is at most only 35% of the full moment determined from bulk

21   measurements[22,25,27] suggesting strong spin fluctuations consistent with a near liquid-like

22   quantum state in the material. (See Supplementary Information for more detail.)

1

2   Having established the structural and magnetic properties of α-RuCl$_3$, we probe the nature of the

3   single-ion states to confirm the presence of strong spin-orbit coupling, which is required to

4   generate the Kitaev term K in (1). By using $E_i = 1.5$ eV incident neutrons to measure the transition

5   from the Ru^{3+} electronic ground state to its excited state the spin-orbit coupling λ is extracted. In

6   the octahedral environment shown in Fig. 1 the ground state is a low-spin (J=1/2) state. The next

7   excited state (J=3/2) is separated by $3\lambda/2$. Neutrons can activate it by a spin-flip process and the

8   transition is seen in Fig. 2 at 195 ± 11 meV implying that $\lambda \approx 130$ meV (also see Supplementary

9   Fig. 4 and Supplementary Information). This is close to the expected free-ion value ($\lambda_{free} \approx 150$

10   meV[20,31]) and the predictions of recent *ab-initio* calculations[26]. The J=3/2 state will be split into

11   two Kramers doublets by small distortions of the octahedron[32,33].   The resolution limited line-

12   width suggests that such a splitting is relatively small, certainly less than the HWHM of 48 meV.

13   In any case, as the higher levels are too energetic to play any role, only the lowest lying doublet

14   needs to be considered.   Projecting the inter-Ru^{3+} couplings into this doublet results in Kitaev

15   terms as included in eqn. (1).

16

17   The above results indicate that the H-K Hamiltonian (1) can indeed satisfactorily capture the

18   interactions between Ru^{3+} moments. If this is the case, then given the highly reduced ordered

19   moment and the extended QSL region close to the observed zigzag AFM phase, it is tempting to

20   speculate that signatures of fractionalization characteristic of QSLs will be manifest in the

21   collective magnetic excitations. Fig. 3 shows data for α-RuCl$_3$ powder measured using neutrons

22   of $E_i = 25$ meV.   The scattering in the magnetically ordered state is shown in Fig. 3a for $T = 5$

K. Two distinct features are clearly visible spanning different energy ranges. The lower among

them, M_1, is centered near 4 meV and shows a minimum near $Q = 0.62$ Å^{-1}, which notably

corresponds to the M point of the honeycomb lattice as expected for a quasi-2D magnetic system

(for 3D behavior a wave-vector $Q = 0.81$ Å^{-1} is anticipated). The white arrow draws attention to

the concave shape of the edge of the scattering, which is expected for magnon excitations in a ZZ

ordered state[15]. This firmly establishes the nature of magnetic order and differentiates it from

other potential states such as a stripy ground state. The second feature is at a higher energy, M_2,

centered near 6.5 meV.

Both features M_1 and M_2 correspond to powder averaged modes which are of magnetic origin as

identified by their wave-vector and temperature dependence. The thermal behavior of these

magnetic modes differs significantly from one to the other. Figure 3b shows the scattering at T =

15 K, just above T_N. It is seen that M_1 softens dramatically and the intensity shifts towards Q =

0. Conversely, M_2 is essentially unaffected. Constant Q cuts through the data are displayed in

Fig. 3c. The centers are at the positions indicated by the labeled dashed lines in Fig. 3a and 3b.

Comparing cuts (A,B) with (C,D) reinforces the collapse and shift of intensity for M_1 above T_N.

Cut B clearly shows two peaks implying that the density of states sampled by the powder

average at T = 5 K has two maxima. The average peak energies determined by fits of the data to

Gaussian peaks are given by $E_1 = 4.1(1)$ meV and $E_2 = 6.5(1)$ meV. Figure 3d shows constant

energy cuts integrated over the range [2.5, 3.0] meV, near the lower edge of M_1. It is seen that at

low temperature M_1 is structured with low energy features showing up as peaks in cut E. These

are centered at $Q_1 = 0.62(3)$ Å^{-1} and $Q_2 = 1.7(1)$ Å^{-1}. Above T_N this structure disappears, and the

7

1   broad scattering shifts dramatically to lower Q. Fitting the $T = 15$ K data (cut F) to a Lorentzian

2   with the center fixed at $Q = 0$ yields a HWHM of roughly 0.6 Å^{-1}, suggesting that above T_N

3   spatial correlations of the spin fluctuations are extremely short ranged.

4

5   To gain further insight into the magnetic couplings we compare the INS data to the solution of

6   (1) using conventional linear spin wave theory (SWT) for ZZ order[34,35]. The SWT provides a

7   quasi-classical approximation which works reasonably well when quantum fluctuations are

8   weak. Although strictly speaking it is inapplicable for strongly quantum fluctuating systems, it

9   provides a first starting point for estimating the approximate and relative strengths of the

10   couplings. In the honeycomb lattice appropriate for α-RuCl$_3$, SWT predicts four branches, two

11   of which disperse from zero energy at the M point ($\frac{1}{2}$, 0) to doubly degenerate energies $\omega_1 =$

12    $\sqrt{K(K + J)}$ and $\omega_2 = |J|\sqrt{2}$ respectively at the Γ point $(0,0)$[34]. A large density of states in the

13   form of van Hove singularities is expected near ω_1 and ω_2. Figure 4a shows the SWT and Fig.

14   4b the calculated powder averaged neutron scattering. Equating ω_1 and ω_2 with the peaks E_1 and

15   E_2 yields K and J values of (K=7.0, J=-4.6) meV (shown in Figure 4) or (K=8.1, J=-2.9) meV

16   (shown in Supplementary Fig. 5) depending on whether ω_1 corresponds to E_1 or E_2. These two

17   possibilities lie on either side of the symmetric point K=-2J, where $\omega_1 = \omega_2$. The inset of Fig. 4d

18   shows each of these possibilities on the H-K phase diagram[34]. Either way the Kitaev term is

19   stronger and antiferromagnetic, while the Heisenberg term is ferromagnetic; again consistent

20   with ab-initio calculations[26].

21

1   We note that the M_1 mode has a gap of at least 1.7 meV near the M point (see Fig. 5a) that is not

2   exhibited in the above SWT calculations. While such a gapless spectrum is a known artifact of

3   linear SWT for the H-K model[34], the experimentally observed gap is too large to be accounted

4   for within systematic 1/S corrections. Extending the Hamiltonian to include further terms can

5   lead to a gap forming within SWT. However, calculations of the SW spectrum (See

6   Supplementary Fig. 5 and Supplementary Information) with additional terms in the Hamiltonian

7   (such as Γ and/or Γ' terms[35-39]), when sufficient to generate the observed gap, show features in

8   the powder averaged scattering that are inconsistent with the observations. Within the SW

9   approximation a gap can also be generated by adding an additional Ising-like anisotropy, perhaps

10   at the level of 15% of J, which is also equivalent to an anisotropic Kitaev interaction. As

11   discussed below, the resulting SWT is still incompatible with the data.

12

13   Although the SWT calculation reproduces many of the features of the observed dynamical

14   response, crucial *qualitative* disagreements remain. Most importantly, the observed dependence

15   of the M_2 mode on temperature and energy is incompatible with linear SWT.   The constant

16   wave-vector cuts shown in Fig. 3c show that M_2 maintains a totally consistent peak shape and

17   intensity above and below T_N. Moreover, for temperatures well above T_N to at least 40 K the

18   intensity for all measured wave-vectors is essentially unchanged as shown by Fig. 5b, which is a

19   plot of the M_2 intensity as a function of Q for several temperatures. In fact a well-defined M_2

20   peak persists with a similar Q dependence up to at least 70 K corresponding to $T \sim 5T_N$. This is

21   in sharp contrast to the typical behavior of spin waves in conventional magnets, which generally

22   exhibit a dramatic decrease of intensity above the ordering temperature.   It should also be noted

9

1   that in the ordered state the energy width of M_2 is much broader than the SW calculation over the

2   observed range of Q. Fig. 5c, shows a constant Q cut around the M_2 mode (blue triangles). The

3   red line shows the equivalent powder averaged SWT calculation (Fig. 4b), broadened by the

4   instrumental energy resolution (marked "R") and scaled so that the intensity matches the height

5   of the M_2 scattering. The low energy side of the calculation is affected by the lower mode and

6   therefore cannot be directly compared with the data, however it is clear from the high energy

7   side that there is considerable extra scattering (indicated by the shading) that is not captured by

8   SWT. As discussed in the supplementary information, the smooth drop off of intensity on the

9   high energy side of the M_2 peak argues against the extra width arising from additional features in

10   the spin wave spectrum that can be achieved by adding extra terms to eqn. (1). Finally, as

11   discussed in the supplementary information, for temperatures above T_N the detailed wave-vector

12   dependence of the scattering is not what is expected from conventional SWT.

13

14   The SWT is a quantization of harmonic excitations from classical order. Moreover, the low

15   ordered moment observed in α-RuCl$_3$ indicates that linear SWT is inadequate.   Indeed, we argue

16   that the behavior of the observed higher energy mode M_2 – which because of its short-time scale

17   is least sensitive to 3D couplings –is naturally accounted for via the QSL phase proximate in the

18   H-K phase diagram[40].

19

20   This QSL viewpoint has the strong quantum limit as its starting point. It can avail itself of the

21   recently computed exact dynamical structure factor of the pure Kitaev model, in which spin

22   excitations fractionalize into static Ising fluxes and propagating Majorana fermions minimally

1 coupled to a Z_2 gauge field[10]. Powder averaged results of the scattering[10] expected for the

2 isotropic antiferromagnetic Kitaev model is shown in Fig. 5d. Although the QSL is gapless, the

3 structure factor of its excitations shown in Fig. 5d does show a gap. This is due to the fact that a

4 spin flip always excites both quasiparticles - gapless Majorana fermions and a pair of Ising

5 fluxes, the latter with a nonzero excitation gap[10]. This results in a low energy band from 0.125-

6 0.5 K with a peak of intensity near the M point in the Brillouin zone for an antiferromagnetic K.

7 Most interestingly, in addition, a second very broad and non-dispersing high energy band

8 appears, centered at an energy that corresponds approximately to the Kitaev exchange scale, K.

9 (For a similar calculation on the ferromagnetic Kitaev model, and a general discussion, see

10 Supplementary Fig. 6. and Supplementary Information)   The intensity of the upper band is

11 strongest at Q = 0 and decreases with increasing Q.

12

13 With the Kitaev interaction dominant it is reasonable to expect that α-RuCl$_3$ is proximate to the

14 QSL phase. The additional non-Kitaev interactions lead to long-range order at low temperatures

15 and strongly affect the low energy excitations, which then exhibit spin-wave behavior.

16 Conversely, the high energy spin fluctuations native to the proximate quantum ground state are

17 more immune, and can persist even in the ordered state.   This behavior is well known in coupled

18 S=1/2 antiferromagnetic Heisenberg chains[6], where at energies large compared to the interchain

19 coupling the spectrum of fractionalized excitations (spinons) of the pure chain dominates the

20 response above and below the magnetic ordering temperature. This leads to a natural

21 interpretation of the M_2 mode as having the same origin as the upper mode of the Kitaev QSL.

22 The broad width of the M_2 mode as seen in the measurements can be naturally explained in terms

1   of the fractionalized Majorana fermion excitations. The green line in Fig. 5c shows the

2   calculated powder averaged QSL scattering including the effects of instrumental resolution, with

3   the value $K = 5.5$ meV chosen to match the experimental peak position of M_2 and the overall

4   height chosen to match the observed scattering. The calculated QSL scattering profile is well-

5   matched to the observed additional width of the M_2 scattering on the high energy side. This

6   value of K is somewhat smaller than that inferred from SWT, but it is very reasonable to expect

7   that the quantum description requires a renormalized parameter. The large energy width is

8   expected for a fractionalized system because several excitations are excited in a single spin flip

9   process. Moreover, the Q dependence of the intensity of the M_2 mode (Fig. 5b) strikingly

10   resembles that of the upper band in the pure Kitaev model. The feature is broad in momentum

11   since the real-space spin correlations of a QSL are short-ranged. For convenience, a side-by-side

12   comparison of the Q dependence of the data and the scattering calculated for SWT and a pure

13   Kitaev model is presented in Supplementary Fig. 7.

14

15   The fact that M_2 survives well above T_N, even if M_1 is completely washed out, indicates that the

16   M_2 mode is not directly connected to the existence of long range magnetic order. In the strictly

17   2D Kitaev model there is no true phase transition from the QSL to the high temperature

18   paramagnet[41]. However, recent Monte Carlo calculations at finite temperature suggest that high

19   energy Majorana fermions, thus the M_2 mode, remain stable up to the highest cross over

20   temperature at an energy scale of K[42], consistent with the observations reported here.

21

1   Taken together, the qualitative features from a complete quantum calculation using a Majorana

2   fermion treatment can successfully provide a broadly consistent account of the inelastic neutron

3   scattering data. This makes α-RuCl$_3$ a prime candidate for realizing Kitaev and QSL physics.

4   Further support for the presence of Kitaev QSL physics in α-RuCl$_3$ is seen in recent Raman

5   scattering measurements[24] which show broad response similar to that calculated for the pure

6   Kitaev model[17] with a value of $K = 8$ meV, of the same order as that derived here. The Raman

7   continuum also persists to temperatures well above T_N. Much more detailed information on the

8   structure of the response functions will require INS in single-crystals of both α-RuCl$_3$ and other

9   relevant compounds, some of which are 3D[43,44]. The most instructive measurements on α-

10   RuCl$_3$ should use single crystals free of the complications induced by stacking faults.

11

12   Ideally, a single fully quantum theoretical treatment should capture the microscopic behavior

13   across all energy and length scales; however, such a treatment is unavailable for the full

14   Hamiltonian describing the magnetic properties of α-RuCl$_3$. Here, we have used the insight that

15   the high-energy short-range spin-liquid physics is well-captured by a pure Kitaev model which

16   permits an analytic treatment, but misses the weak ordering tendency due to perturbations to the

17   simple model Hamiltonian. These, however, and their concomitant low-energy spin wave

18   excitations can be approximately captured by SWT. Considering the usual renormalizations

19   inherent in semiclassical descriptions of quantum excitations, these two approximation schemes

20   for different parts of the spectrum can be described by similar microscopic parameters,

21   suggesting that the absence of a full treatment of the complete H-K model is a technical rather

22   than conceptual issue.

1

2 Looking forward, it will also be of great interest to systematically investigate the effects of

3 disorder and doping in these materials[45], and there is also the hope of generating a genuinely

4 two-dimensional system by exfoliation techniques.

5

6 **Methods:**

7 **Synthesis and bulk measurements:** Commercial-$RuCl_3$ powder was purified in-house to a

8 mixture of α-$RuCl_3$ and β-$RuCl_3$, and converted to 99.9% phase pure α-$RuCl_3$ by annealing at

9 500 °C. Single-crystals of α-$RuCl_3$ were grown using vapor transport with $TeCl_4$ as the

10 transport agent. The crystals exhibit an anisotropic mosaic for in-plane peaks, indicative of

11 stacking faults, as shown in Supplementary Fig. 2. Samples were characterized by standard bulk

12 techniques (see Supplementary Fig. 1). X-ray powder diffraction was carried out at room

13 temperature using a Panalytical Empyrian diffractometer employing Cu K_α radiation.

14 The structure was found to be consistent with the trigonal space group $P3_112$ (No. 151) with

15 room-temperature lattice constants $a=b=5.9783(2)$ Å, $c=17.170(1)$ Å with $\chi^2 = 13.7$ and wRp =

16 5.16. For $C2/m$ the corresponding fits are worse, with $a = 5.982(1)$, $b=10.3530(7)$, $c=6.0611(5)$,

17 $\beta=109.177(7)$ with $\chi^2 = 16.9$, wRp = 6.33. In addition, powder neutron diffraction was carried

18 out at 10 K. For the fit and the lattice constants at T = 10 K refer to Supplementary Fig. 2 and

19 Supplementary Table 2. Magnetic properties were measured with a Quantum Design (QD)

20 Magnetic Property Measurement System in the temperature interval 1.8 K ≤ T ≤ 300 K.

21 Temperature-dependent specific heat data were collected using a 14 T QD Physical Property

14

1 Measurement System (PPMS) in the temperature range from 1.9 to 200 K. Our measurements of

2 the susceptibility (see Supplementary Fig. 1) are consistent with existing literature[22,25,27.] The

3 magnetic susceptibility of powders fits a Curie-Weiss law over the range above 150 K, with a

4 temperature intercept of $\theta \approx 32$ K and a single-ion Ru effective moment of 2.2 μ_B. Magnetic

5 order appears for $T \leq 15$ K leading to a broad specific heat anomaly. The detailed specific heat

6 of single-crystal specimens is sample dependent, but consistent with other groups[25,27,29], and

7 shows the onset of a broad anomaly near 14 K, and a sharper peak near 8 K, possibly with

8 additional structure in between those temperatures. This complicated behavior is a consequence

9 of stacking faults (see main text).

10 **Neutron Diffraction:** Neutron diffraction data for structural refinement on a 5.1 g powder

11 sample of α-RuCl$_3$ were collected at the POWGEN beamline at the Spallation Neutron Source

12 (SNS), at Oak Ridge National Laboratory (ORNL). The sample was loaded in a vanadium

13 sample can under helium, and measured at $T \approx 10$ K. Neutron diffraction measurements to

14 characterize the magnetic Bragg peaks in both powder and single-crystals was performed at the

15 HB-1A Fixed Incident Energy (FIE-TAX, $E_i = 14.68$ meV) triple-axis instrument at the High-

16 Flux Isotope Reactor at ORNL.   For powder diffraction, 4.7 g of powder was packed into a

17 cylindrical aluminum canister. For single-crystal diffraction, one ~0.7 x 1.0 cm^2, 22.5 mg crystal

18 was attached to a flat aluminum shim using Cytop-M glue. It was then sealed with indium into an

19 aluminum canister with helium exchange gas and then aligned and confirmed to be a single-

20 domain sample using neutrons. This was attached to the cold-finger of a 4 K closed-cycle

21 refrigerator for performing the temperature scans.

22

1   **Inelastic neutron scattering:** Inelastic neutron scattering of powder α-RuCl$_3$ was performed

2   using the SEQUOIA chopper spectrometer at the SNS[46]. The sample (5.3 grams) was sealed at

3   room temperature in a 5 x 5 x 0.2 cm^3 flat aluminum sample can using helium exchange gas for

4   thermal contact. This was mounted to the cold finger of a closed cycle helium refrigerator for

5   temperature control. Empty can measurements were performed under the same conditions as the

6   sample measurements. All inelastic data have been normalized to the incident proton charge and

7   have the empty can background subtracted. Measurements were made with E_i=8, 25, and 1500

8   meV for the neutron incident energies. The E_i=8 and 25 meV measurements were performed

9   using the fine resolution 100 meV Fermi chopper slit package spinning at 180 Hz and the T_0

10   chopper spinning at 30 Hz. The E_i=1500 meV measurements used the 700 meV coarse

11   resolution Fermi chopper spinning at 600 Hz and the T_0 chopper spinning at 180 Hz[47]. The

12   E_i=1500 meV configuration yields a calculated full width at half maximum (FWHM) energy

13   resolution of approximately 97 meV at 200 meV energy transfer. The FWHM elastic energy

14   resolution is calculated to be 0.19 and 0.64 meV for the E_i = 8 and 25 meV configurations

15   respectively. Care was taken to minimize the exposure of the sample to air, and after every

16   exposure the sample was pumped for at least 30 minutes to remove adsorbed moisture. Structural

17   refinements confirmed the purity of the powder sample. Spin wave simulations were performed

18   using SpinW codes[48] (Version 235) and used the nominal symmetric honeycomb structure for α-

19   RuCl$_3$[21,22]. The SWT powder average was performed with 3000 random points distributed over

20   the Brillouin zone. The Ru^{3+} form factor utilized was interpolated using the results of relativistic

21   Dirac-Slater wave functions[49].

22

References:

1. Balents, L., Spin Liquids in Frustrated Magnets. *Nature* **464**, 199-208 (2010).

2. Lee, P. A., An End to the Drought of Quantum Spin Liquids. *Science* **321**, 1306-1307 (2008).

3. Yamashita, M. *et al*, Highly Mobile Gapless Excitations in a Two-Dimensional Candidate Quantum Spin Liquid. *Science* **328**, 1246-1248 (2010).

4. Sachdev, S., Quantum magnetism and criticality. *Nature Physics* **4**, 173-185 (2008).

5. Nayak, C., Simon, S. H., Stern, A., Freedman, M. & Sharma, S. D., Non-Abelian anyons and topological quantum computation. *Rev. Mod. Phys.* **80**, 1083-1159 (2008).

6. Lake, B., Tennant, D. A., Frost, C. D. & Nagler, S. E., Quantum Criticality and universal scaling of a quantum antiferromagnet. *Nature Materials* **4**, 329-334 (2005).

7. Han, T.-H., *et al*., Fractionalized excitations in the spin-liquid state of a kagome-lattice antiferromagnet. *Nature* **492**, 406-410 (2012).

8. Kitaev, A., Anyons in an exactly solved model and beyond. *Annals of Phys.* **321**, 2-111 (2006).

9. Baskaran, G., Mandal, S., & Shankar, R., Exact Results for Spin Dynamics and Fractionalization in the Kitaev Model. *Phys. Rev. Lett.* 98, 247201 (2007).

1   10. Knolle, J., Kovrizhin, D. L., Chalker, J. T. & Moessner, R., Dynamics of a Two-

2   Dimensional Quantum Spin Liquid: Signatures of Emergent Majorana Fermions and Fluxes.

3   *Phys. Rev. Lett.* **112**, 207203 (2014).

4   11. Jackeli, G. & Khaliullin, G., Mott Insulators in the Strong Spin-Orbit Coupling Limit: From

5   Heisenberg to a Quantum Compass and Kitaev Models, *Phys. Rev. Lett.* **102**, 017205

6   (2009).

7   12. Chaloupka, J., Jackeli, G. & Khaliullin, G., Kitaev-Heisenberg Model on a Honeycomb

8   Lattice: Possible Exotic Phases in Iridium Oxides A_2IrO_3. *Phys. Rev. Lett.* **105**, 027204

9   (2010).

10 13. Kim, B. J. *et al.*, Phase-Sensitive Observation of a Spin-Orbital Mott State in Sr_2IrO_4.

11   *Science* **323**, 1329-1332 (2009).

12 14. Singh, Y. *et al.*, Relevance of the Heisenberg-Kitaev Model for the Honeycomb Lattice

13   Iridates A_2IrO_3. *Phys. Rev. Lett.* **108**, 127203 (2012).

14 15. Choi, S. K. *et al.*, SpinWaves and Revised Crystal Structure of Honeycomb Iridate Na_2IrO_3.

15   *Phys. Rev. Lett.* **108**, 127204 (2012).

16 16. Ye, F. *et al.*, Direct evidence of a zigzag spin-chain structure in the honeycomb lattice: A

17   neutron and x-ray diffraction investigation of single-crystal Na_2IrO_3. *Phys. Rev. B* **85**,

18   180403(R) (2012).

1 17. Knolle, J., Chern, G.-W., Kovrizhin, D. L., Moessner, R. & Perkins, N. B., Raman

2 Scattering Signatures of Kitaev Spin Liquids in A_2IrO_3 Iridates with A = Na or Li. *Phys.*

3 *Rev. Lett.* **113**, 187201 (2014).

4 18. Gretarsson, H. *et al.*, Magnetic excitation spectrum of Na_2IrO_3 probed with resonant

5 inelastic x-ray scattering. *Phys. Rev. B* **87**, 220407(R) (2013).

6 19. Chun, S.H. *et al.*, Direct evidence for dominant bond-directional interactions in a

7 honeycomb lattice iridate Na_2IrO_3. *Nature Phys.* 11, 462 (2015).

8 20. Figgis, B. N., Lewis, J., Mabbs, F. E. & Webb, G. A., Magnetic Properties of Some Iron(III)

9 and Ruthenium(III) Low-spin Complexes. *J. Chem. Soc.* **A**, 422 - 426 (1966).

10 21. Fletcher, J. M. *et al.*, Anhydrous Ruthenium Chlorides. *Nature* **199**, 1089-1090 (1963).

11 22. Fletcher, J. M., Gardner, W. E., Fox, A. C. & Topping, G., X-Ray, Infrared, and Magnetic

12 Studies of α- and β-Ruthenium Trichloride. *Journal of Chem. Society* **A**, 1038-1045 (1967).

13 23. Plumb, K. W. *et al.*, α-$RuCl_3$: A spin-orbit assisted Mott insulator on a honeycomb lattice.

14 *Phys. Rev. B* **90**, 041112(R) (2014).

15 24. Sandilands, L. J. *et al.*, Scattering Continuum and Possible Fractionalized Excitations in α-

16 $RuCl_3$. *Phys. Rev. Lett.* **114**, 147201 (2015).

17 25. Sears, J. A. *et al.*, Magnetic order in α-$RuCl_3$: a honeycomb lattice quantum magnet with

18 strong spin-orbit coupling. *Phys. Rev. B* **91**, 144420 (2015).

19

26. Shankar, V. V., Kim, H.-S. & Kee, H.-Y., Kitaev magnetism in honeycomb $RuCl_3$ with intermediate spin-orbit coupling, *Phys. Rev. B* **91**, 241110 (2015).

27. Majumder, M. *et al.*, Anisotropic Ru^{3+} $4d^5$ magnetism in the α-$RuCl_3$ honeycomb system: susceptibility, specific heat and Zero field NMR. *Phys. Rev. B* **91**, 180401(R) (2015).

28. Sandilands, L. J. *et al.*, Orbital excitations in the 4d spin-orbit coupled Mott insulator α-$RuCl_3$, Available at http://arxiv.org/abs/1503.07593 (2015). Phys. Rev. B *(accepted)*.

29. Kubota, Y., Tanaka, H., Ono, T., Narumi, Y. & Kindo, K., Successive magnetic phase transitions in α-$RuCl_3$: XY-like frustrated magnet on the honeycomb lattice. *Phys. Rev. B* **91**, 094422 (2015).

30. Krumhansl, J., & Brooks, H., The Lattice Vibration Specific Heat of Graphite. *J. Chem. Phys.* **21**, 1663 (1953).

31. Abragam, A. & Bleaney, B., *Electron Paramagnetic Resonance of Transition Ions* (Oxford University Press, London, 1970).

32. Stevens, K. W. H., On the magnetic Properties of covalent XY_6 complexes. *Proc. Phys. Soc. A* (219) 542-555 (1953).

33. Perkins, N. B., Sizyuk, Y. & Wölfle, P., Interplay of many-body and single-particle interactions in iridates and rhodates. *Phys. Rev. B* **89**, 035143 (2014).

34. Chaloupka, J., Jackeli, G. & Khaliullin, G., Zigzag Magnetic Order in the Iridium Oxide Na_2IrO_3. *Phys. Rev. Lett.* **110**, 097204 (2013).

35. Rau, J. G. & Kee, H.-Y., Trigonal distortion in the honeyccomb iridates: Proximity of zigzag and spiral phases in Na_2IrO_3, Available at http://arxiv.org/abs/1408.4811 (2014).

36. Rau, J. G., Lee, E. K.-H. & Kee, H.-Y., Generic Spin Model for the Honeycomb Iridates beyond the Kitaev Limit. *Phys. Rev. Lett.* **112**, 077204 (2014).

37. Sizyuk, Y., Price, C., Wolfle, P. & Perkins, N. B., Importance of anisotropic exchange interactions in honeycomb iridates: Minimal model for zigzag antiferromagnetic order in Na_2IrO_3. *Phys. Rev. B* **90**, 155126 (2014).

38. Katukuri, V. M. *et al.*, Kitaev interactions between j = 1/2 moments in honeycomb Na_2IrO_3 are large and ferromagnetic: insights from *ab initio* quantum chemistry calculations. *New J. Phys.* **16**, 013056 (2014).

39. Chaloupka, J. & Khaliullin, G., Hidden symmetries of the extended Kitaev-Heisenberg model: Implications for honeycomb lattice iridates A_2IrO_3, *Phys. Rev. B* **92**, 024413 (2015).

40. Alpichshev, Z., Mahmood, F., Cao, G. & Gedik, N., Confinement-Deconfinement Transition as an Indication of Spin-Liquid-Type Behavior in Na_2IrO_3. *Phys. Rev. Lett.* **114**, 017203 (2015).

41. Nasu, J., Udagawa, M. & Motome, Y., Vaporization of Kitaev Spin Liquids. *Phys. Rev. Lett.* **113**, 197205 (2014).

42. Nasu, J., Udagawa, M. & Motome, Y., Thermal Fractionalization of Quantum Spins in a Kitaev Model, *Phys. Rev. B* **92**, 115122 (2015).

1 43. Modic, K. A. *et al.*, Realization of a three-dimensional spin–anisotropic harmonic

2   honeycomb iridate. *Nature Communications* **5**, 4203 (2014).

3 44. Takayama, T. *et al.*, Hyperhoneycomb Iridate $\beta-Li_2IrO_3$ as a Platform for Kitaev

4   Magnetism. *Phys. Rev. Lett.* **114**, 077202 (2015).

5 45. Zschocke, F. & Vojta, M., Physical states and finite-size effects in Kitaev's honeycomb

6   model: Bond disorder, spin excitations, and NMR lineshape, *Phys. Rev. B* **92**, 014403

7   (2015).

8 46. Granroth, G. E. *et al.*, SEQUOIA: a newly operating chopper spectrometer at the SNS.

9   *Journal of Physics: Conference Series* **251**, 12058 (2010).

10 47. Abernathy, D. L. *et al.*, Design and operation of the wide angular range chopper

11   spectrometer ARCS at the SNS. *Review of Scientific Instruments* **83**, 15114 (2012).

12 48. Toth, S. & Lake, B., Linear spin wave theory for single-Q incommensurate magnetic

13   structures. *J. Phys. Condens. Matter* **27**, 166002 (2014).

14 49. Cromer, D. T. & Weber, J. T., Scattering Factors Computed From Relativistic Dirac-Slater

15   Wave Functions. *LANL REPORT LA-3056* (1964).

16

1   **Supplementary Information:**

2

3   Supplementary information is linked to the online version of the paper.

4

5   **Acknowledgements:**

6

21

22   **Author contributions:**

23

S.N., A.B. and D.G.M. conceived the project and the experiment. C.B., L.L., A.B., J-Q.Y., Y.Y., and D.G.M. made the samples. J-Q.Y., L.L., A.B. and C.B. performed the bulk measurements, A.B., A.A., M.B.S., G.E.G, M.L. and S.N. performed INS measurements, A.B., S.N., C.B., M.L., M.B.S. and D.A.T. analyzed the data. Further modeling and interpreting of the neutron scattering data was carried out by A.B., M.L., S.N., J. K., S.B., D.K. and R.M.. A.B., M.L., S.B. and S.N. performed SWT simulations, and J. K., S.B., D.K. and R.M. carried out QSL theory calculations. A.B. and S.N. prepared the first draft, and all authors contributed to writing the manuscript.

Author affiliations:

Quantum Condensed Matter Division, Oak Ridge National Laboratory, Oak Ridge, TN 37830, U.S.A.: A. Banerjee, A.A. Aczel, M.B. Stone, G.E. Granroth, M.D. Lumsden and S.E. Nagler.

Chemical Sciences Division, Oak Ridge National Laboratory, Oak Ridge, TN 37830, U.S.A.: C.A. Bridges.

Material Sciences and Technology Division, Oak Ridge National Laboratory, Oak Ridge, TN 37830, U.S.A.: J-Q. Yan and D.G. Mandrus.

Department of Materials Science and Engineering, University of Tennessee, Knoxville, TN 37996, U.S.A.: J-Q. Yan and D.G. Mandrus.

1   **Neutron Data Analysis & Visualization Division, Oak Ridge National Laboratory, Oak**

2   **Ridge, TN 37830, U.S.A.:** G.E. Granroth

3   **Department of Physics, University of Tennessee, Knoxville, TN 37996, U.S.A.:** Y. Yiu

4   **Department of Physics, Cavendish Laboratory, J.J. Thomson Avenue, Cambridge CB3**

5   **0HE, U.K.:** J. Knolle and D.L. Kovrizhin.

6   **Max Planck Institute for the Physics of Complex Systems, D-01187 Dresden, Germany.:** S.

7   Bhattacharjee and R. Moessner.

8   **Neutron Sciences Directorate, Oak Ridge National Laboratory, Oak Ridge, TN 37830,**

9   **U.S.A.:** D.A. Tennant.

10   **Bredesen Center, University of Tennessee, Knoxville, TN 37966, U.S.A.:** S.E. Nagler

11   **International Center for Theoretical Sciences, TIFR, Bangalore 560012, India.:** S.

12   Bhattacharjee

13

14   **Author statement:**

16   **Corresponding author statement:**

1   Readers are welcome to comment on the online version of the paper. Correspondence and

2   requests for materials should be addressed to: Arnab Banerjee (banerjeea@ornl.gov) and Stephen

3   E. Nagler (naglerse@ornl.gov).

a

$\alpha - RuCl_3$

Ru
Cl

b

β

γ

α

a

b

c

b=5.97 Å

c = 17.2 Å

d

C_p, H = 0

C_p (J/mol K)

60

40

20

0

0   50   100   150   200

T(K)

3

0

6   12   18

e

Powder
Q = 0.81 Å^{-1}
(1/2 0 3/2)

Counts/sec.

26

25

24

f

(1/2 0 1)
(1/2 0 3/2)

Counts/sec

2

1.5

1

0.7

3   6   9   12   15   18

T (K)

3 mm
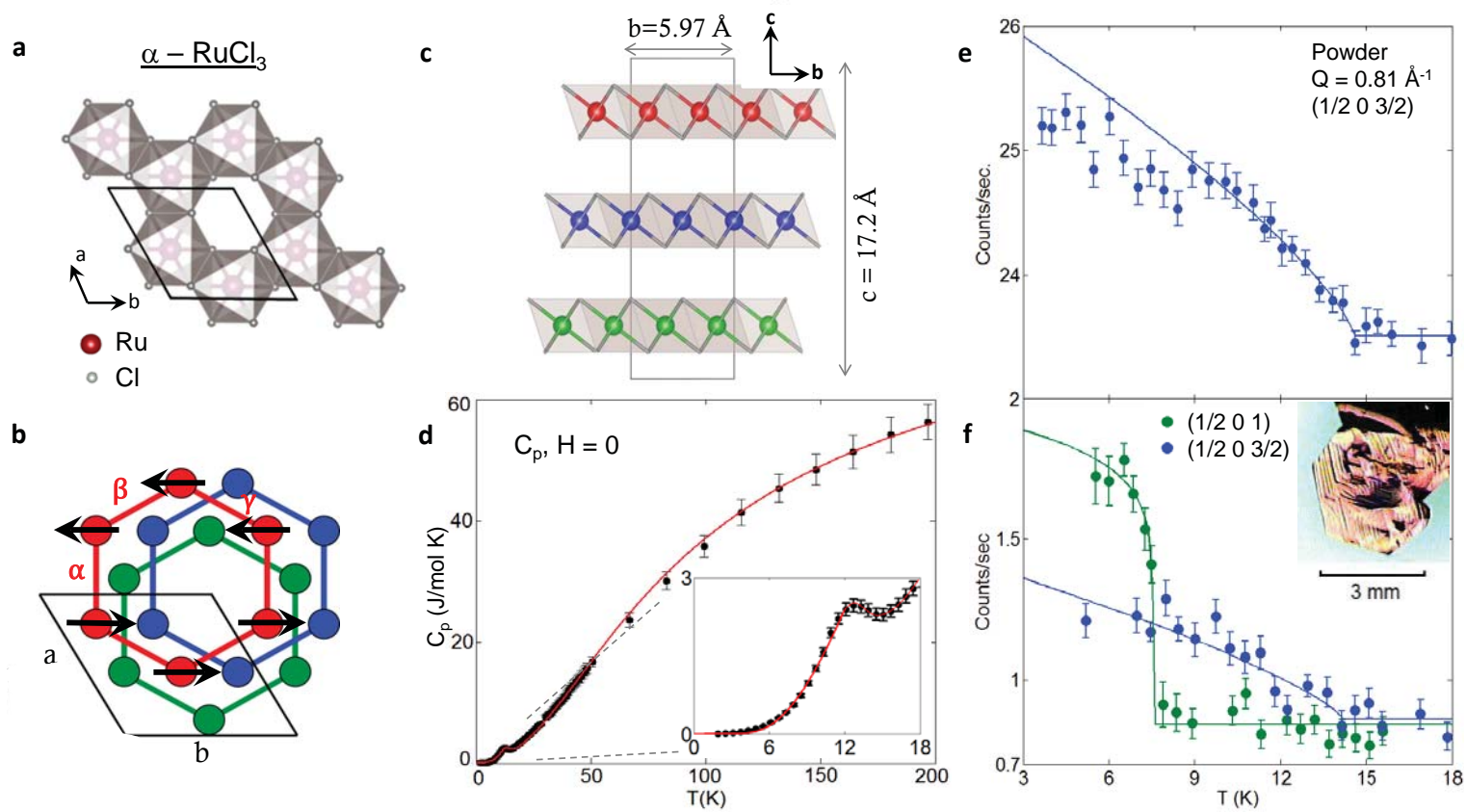
Figure 1

Figure 1: Structure and Bulk properties of 2D layered α-RuCl₃. a-c, The structure of α-

RuCl₃ (space group No. 151, *P3₁12*). **a,** In-plane honeycomb structure showing edge-sharing

RuCl₆ octahedra and the unit cell of the honeycomb lattice. **b,** View along the *c* axis showing the

stacking of honeycomb layers in the unit cell, with Ru atoms in each layer denoted by the colors

red, blue or green. The different intra-layer Ru-Ru bonds, corresponding to the index "*m*" in

equation (1), are labeled in the red layer as α, β, or γ, each with distance *a*/ √3. The two-

dimensional zig-zag magnetic structure is illustrated by the black spins on the red layer. **c,** Side

view of the unit cell showing the offsets along the *c* axis. Values noted are for room temperature

lattice constants. **d,** Specific heat of powder α-RuCl₃. The solid red line is a fit of the data

following the two-dimensional Debye model $C_p(T) = ANk \left(\frac{T}{\theta_D}\right)^2 \int_0^{\frac{\theta_D}{T}} \frac{x^2}{e^x - 1} dx$ for T > 16 K, and

for T < 16 K an empirical function describing the anomaly associated with magnetic order. The

inset in Fig. 1d shows a close-up of the anomaly associated with the low temperature magnetic

ordering transition at $T_N \approx 14$ K in powder samples. (See Extended Data Fig. 1 for more details

of thermodynamic measurements). **e,** Order parameter plot of the (1/2 0 3/2) magnetic Bragg

peak (Q= 0.81 Å⁻¹) in powder samples. The solid blue line is a power-law fit to the data above 9

K yielding T_N = 14.6(3) K, with β = 0.37(3). **f,** Similar plot for single-crystals showing two

coexisting ordering wave-vectors (1/2 0 1) with T_{N1} = 7.6(2) K (green) and (1/2 0 3/2) with T_{N2} =

14.2(8) K (blue). Note that the (1/2 0 1) peak loses intensity sharply, as compared to the (1/2 0

3/2). Inset: picture of the single-crystal (22.5 mg) used in these measurements.

a
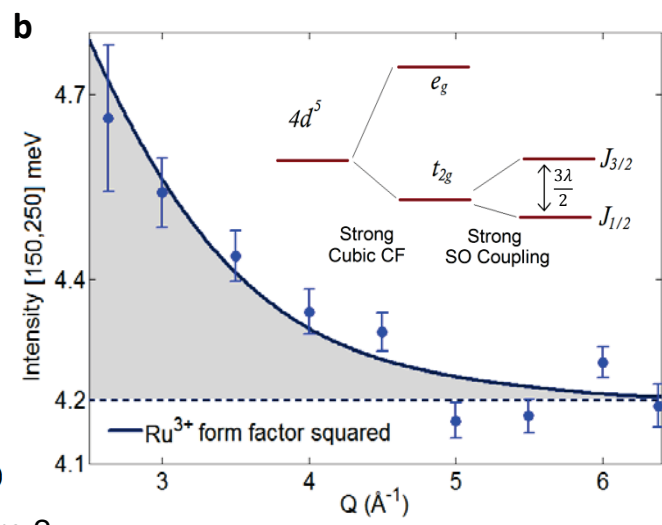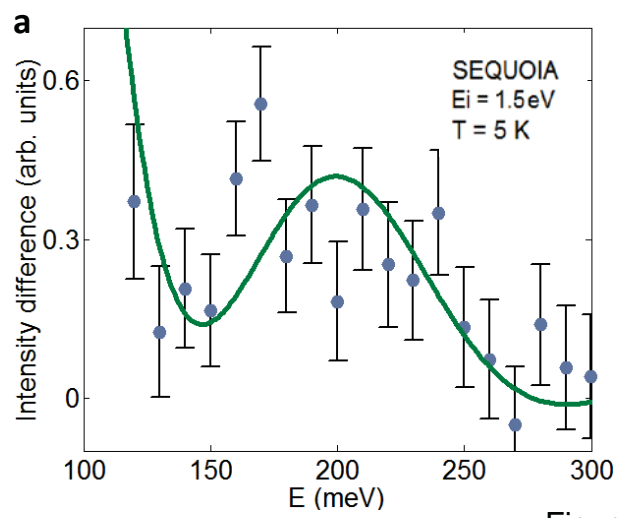
Intensity difference (arb. units)

SEQUOIA
Ei = 1.5eV
T = 5 K

E (meV)

b

Intensity [150,250] meV

$4d^5$

e_g

t_{2g}

$J_{3/2}$

$\frac{3\lambda}{2}$

$J_{1/2}$

Strong
Cubic CF

Strong
SO Coupling

Q (Å^{-1})

— Ru^{3+} form factor squared

Figure 2

Figure 2: Spin-orbit coupling mode in α-RuCl₃, measured at T = 5K with incident energy E_i = 1.5 eV. a, Difference between data integrated over the ranges $Q = [2.5, 4.0]$ Å^{-1} and $[4.5, 6.0]$ Å^{-1} shown in Extended Data Fig. 4, subtracted point by point, illustrating the enhanced signal at low Q. The solid line is a fit to a background plus a Gaussian peak centered at 195 ± 11 meV with HWHM 48 ± 6 meV. With the settings used for the measurement the width is resolution limited. **b,** Intensity for various values of wave-vector integrated over the energy range $[150, 250]$ meV (each point represents a summation in Q over 0.5 Å^{-1} except for the first point which is over 0.26 Å^{-1}). The solid line shows a two parameter fit of the data to the equation $A \cdot |f^{mag}(Q)|^2 + B$, where $f^{mag}(Q)$ is the Ru^{3+} magnetic form factor in the spherical approximation. The shaded area represents the contribution arising from magnetic scattering. Inset: A schematic of the single-ion energy levels for d^5 electrons in the strong octahedral field (i.e., low spin) limit with spin-orbit coupling showing the $J_{1/2}$ to $J_{3/2}$ transition at energy $3\lambda/2$.
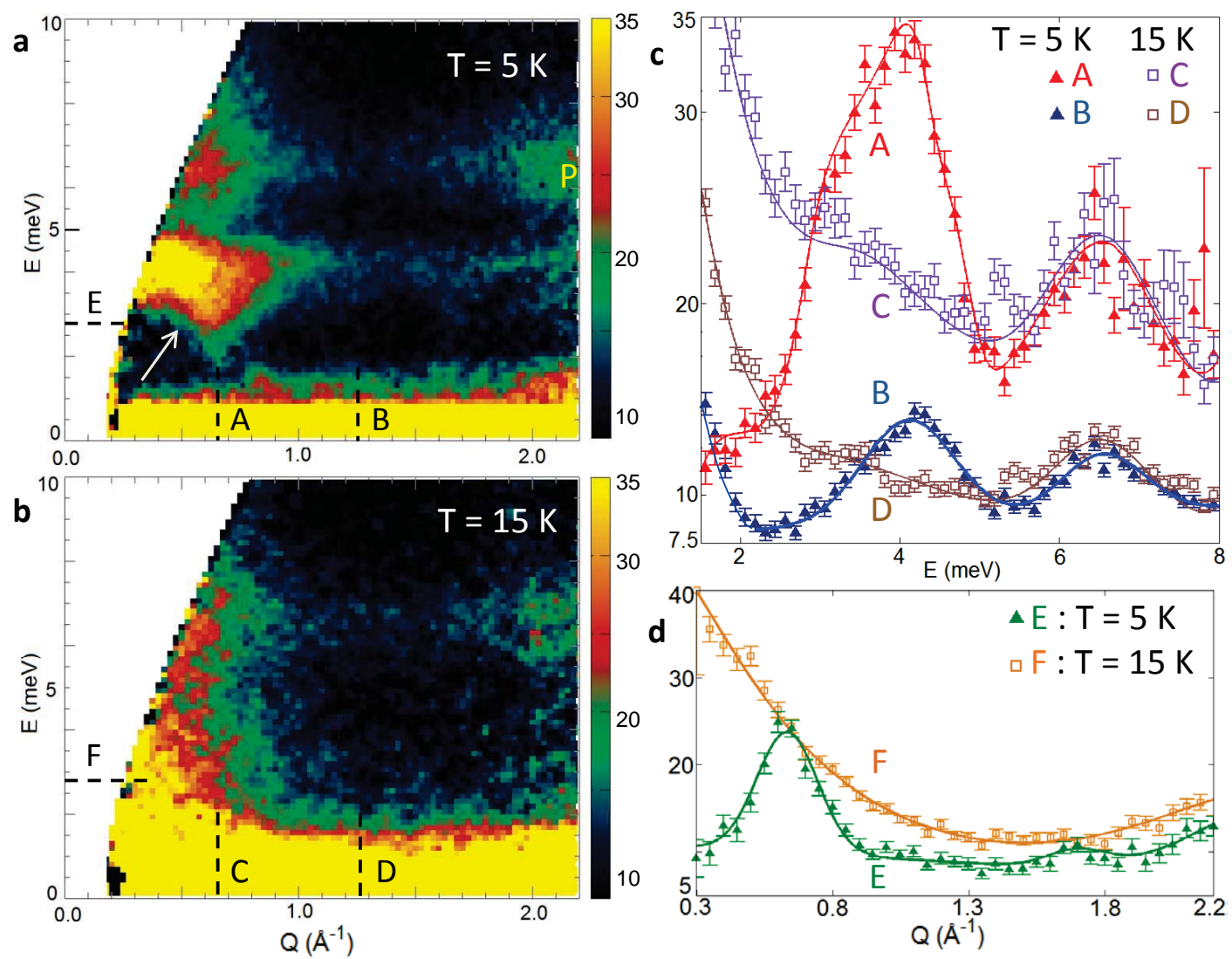
Figure 3

Figure 3: Collective magnetic modes measured using 25 meV incident neutrons. a, False color plot of the data at T = 5 K showing magnetic modes (M_1 and M_2) with band centers near E = 4 and 6 meV. M_1 shows an apparent minimum near Q = 0.62 Å^{-1}, close to the magnitude of the M point of the honeycomb reciprocal lattice. The white arrow shows the concave lower edge of the M_1 mode. The yellow "P" denotes a phonon that contributes to the scattering at an energy near that of M_2, but at higher wave-vectors of Q > 2 Å^{-1}. **b,** The corresponding plot above T_N at T = 15 K shows that M_1 has disappeared leaving strong quasi-elastic scattering at lower values of Q and E. **c,** Constant-Q cuts through the scattering depicted in Fig. 3a and 3b centered at wave-vectors indicated by the dashed lines. The cuts A and C are summed over the range [0.5, 0.8] Å^{-1} which includes the M point of the 2D reciprocal lattice, while B and D span [1.0, 1.5] Å^{-1}. The data from 2 – 8 meV in cut B is fit (solid blue line) to a pair of Gaussians yielding peak energies E_1 = 4.1(1) meV and E_2 = 6.5(1) meV. The solid lines through cuts A, C and D are guides to the eye. **d,** Constant-E cuts integrated over the energy range [2.5, 3.0] meV, at 4 K (E) and 15 K (F). See text for detail. All intensities are in arbitrary units in all panels.
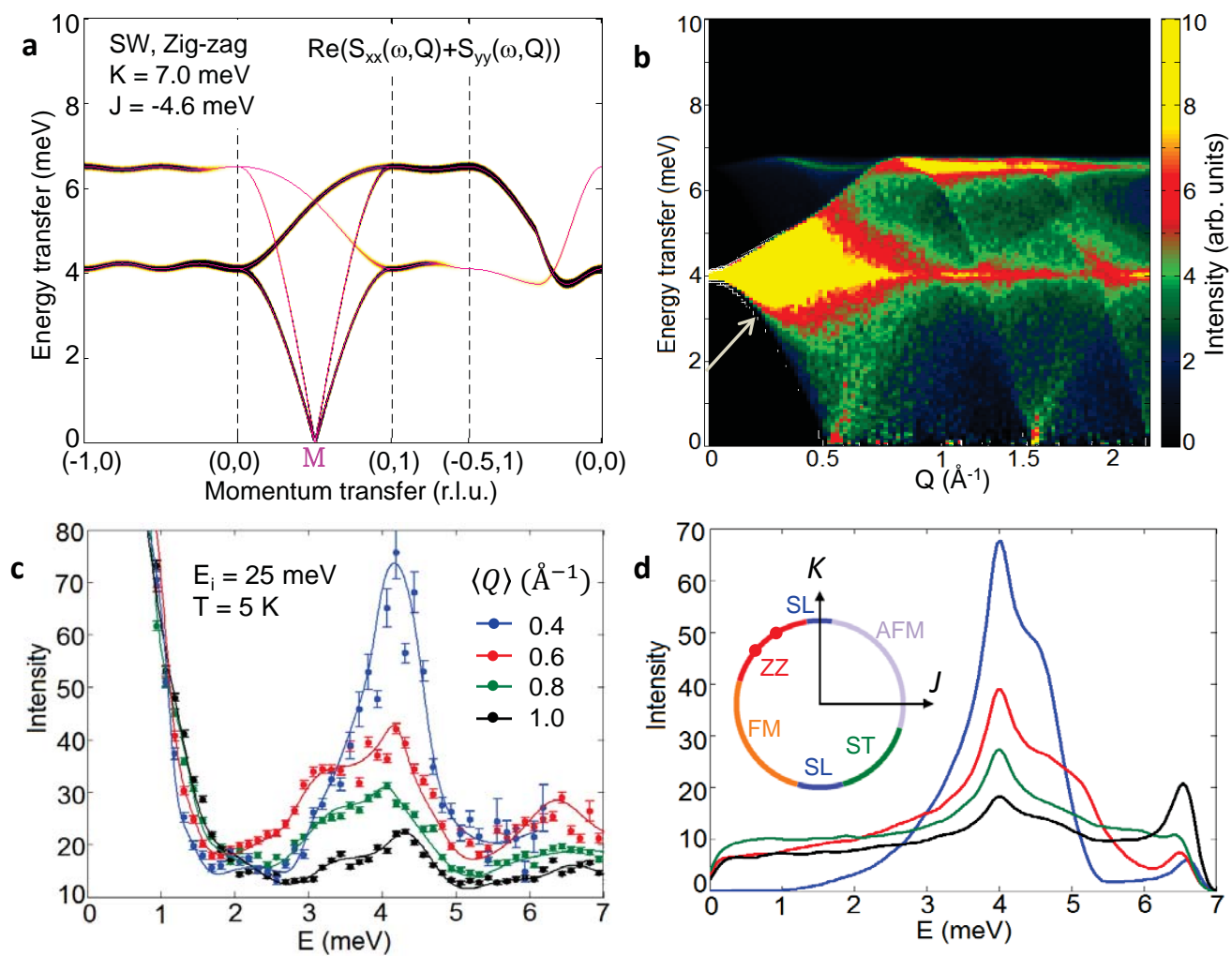
Figure 4

Figure 4: Spin Wave Theory calculations. a, Spin wave simulation for H-K model with (K, J) = (7.0, -4.6) meV with a ZZ ground state. The lattice is the honeycomb plane appropriate for the $P3_112$ space group. **b,** The calculated powder averaged scattering including the magnetic form factor. The white arrow shows the concave nature of the edge of the lower mode in (Q, E) space, similar to the data in Fig. 3a. **c,** Cuts through the data of Fig. 3a integrated over 0.2 Å^{-1} wide bands of wave-vector centered at the values shown. Lines are guides to the eye. Note that actual data includes a large elastic response from Bragg and incoherent scattering. **d,** The same cuts, through the calculated scattering shown in Fig. 4b. Inset: Phase diagram of the H-K model, after Ref. 33. The various phases are denoted by different colors: spin liquid (SL, blue), antiferromagnetic (AFM, light violet), stripy (ST, green), ferromagnetic (FM, orange), and zig-zag (ZZ, red). The red dots represent the two solutions for α-RuCl$_3$ as determined by the zone center spin wave mode energies.
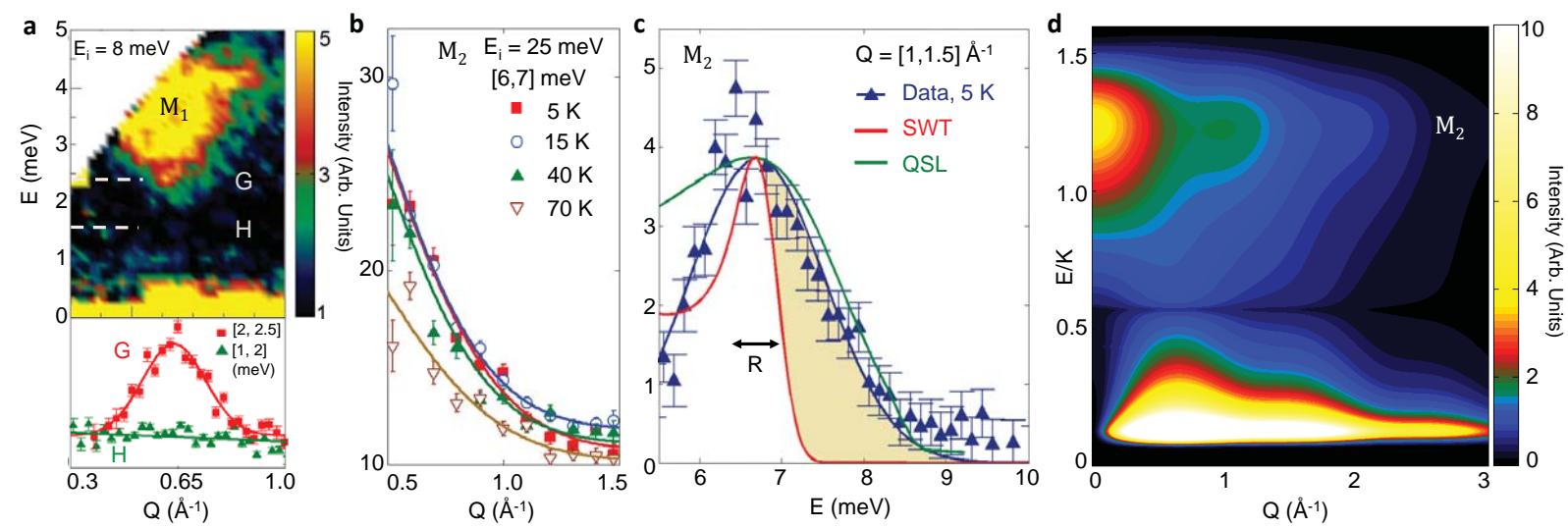
Figure 5

Figure 5: Disagreements with classical SWT and agreement with QSL calculations. a,
Scattering from mode M_1 measured at $T = 5$ K using $E_i = 8$ meV. Lower panel shows constant energy cuts over the energy ranges shown, centered at the locations labeled (G,H) in the upper panel. The absence of structured scattering below 2 meV confirms the gap in the magnetic excitation spectrum. **b,** Constant-E cuts of the data through the upper mode at four different temperatures, of which one curve at $T = 5$ K is below T_N (red squares) and rest above T_N. The lines are guides to the eye. **c,** A constant-Q cut of the $E_i = 25$ meV, $T = 5$ K data in the Q range shown. The blue triangles show the M_2 portion of the cut B in Fig. 3c, but with the linear background term subtracted, and the blue line is a fit to a Gaussian peak. As discussed in the text, the red line shows simulated SWT scattering and the green line shows the scattering calculated from a Kitaev QSL response function. The shaded area represents magnetic scattering that is not captured by the SWT. The double-ended arrow marked "R" shows the FWHM of the instrumental resolution of 0.5 meV at 6.5 meV. **d,** The powder average scattering calculated from a 2D isotropic Kitaev model, with antiferromagnetic K, using the results of Ref. 10, including the magnetic form factor. The upper feature is broad in energy and decreases in strength largely monotonically as Q increases.

| Stacking	(H K L)	Stripy	ZZ	Data
AB-AB	(1/2 0 3/2)			_25 ± 2_
	(3/2 0 1/2)			_1 ±2_
	Ratio	0.44	0	_0.02 ± 0.07_
ABC-ABC	(1/2 0 1)			_50 ± 4_
	(3/2 0 1)			_4 ± 4_
	Ratio	0.47	0	_0.09 ± 0.07_

Supplementary Table 1

Supplementary Table 1: Comparison of the expected intensities from a stripy and zig-zag order, with the observed intensities from single-crystal diffraction. The ratio of the calculated intensities at the (1/2 0 L) positions with the (3/2 0 L) positions for L = 1 and 3/2 are shown for zig-zag and stripy orders, corrected for both the Lorentz factor and the Ru^{3+} form factor. For the zig-zag order in a perfect honeycomb lattice, the shown (3/2 0 L) locations are forbidden[15]. The observed neutron diffraction intensities are shown. The observed neutron diffraction intensity ratio for the (1/2 0 L) and (3/2 0 L) locations are almost zero, which suggests zig-zag ordering.

| Space group		$P3_1 12$	$C2/m$
Lattice parameters	a (Å)	5.9632(1)	5.9230(3)
	b (Å)	5.9632(1)	10.3291(4)
	c (Å)	17.033(7)	6.011(3)
	β (º)	90	109.14(5)
	V (Å³)	524.56(4)	349.72(3)
Fractional Coordinates	Ru1 x	0.221(1)	0
	Ru1 y	0.443(2)	0.1677(4)
	Ru1 z	1\6	0
	Ru2 x	0.559(2)	
	Ru2 y	0.117(3)	
	Ru2 z	1\6	
	Cl1 x	0.214(2)	0.2300(6)
	Cl1 y	0.453(1)	0
	Cl1 z	0.4224(2)	0.2340(6)
	Cl2 x	0.562	0.2492(4)
	Cl2 y	0.108	0.1718(2)
	Cl2 z	0.422	-0.2337(3)
	Cl3 x	0.870(2)	
	Cl3 y	0.764(1)	
	Cl3 z	0.4220(2)	
wRp		5.41	5.31
χ^2		35.71	34.33
ADP (U_{iso})	Ru1	0.0002(3)	0.0004(2)
	Ru2	0.0002(3)	
	Cl1	0.0026(2)	0.0031(1)
	Cl2	0.0026(2)	0.0031(1)
	Cl3	0.0026(2)	

.

Supplementary Table 2

Supplementary Table 2: Rietveld refinement results for both P3$_1$12 and C2/m structural models of α-RuCl$_3$ at low temperature. The fitted parameters obtained using GSAS are shown for the data obtained on the POWGEN beamline of SNS for Bank 2 (TOF data using λ_{center} = 1.066 Å) at T = 10 K. The systematic uncertainties introduced by stacking faults prevent the GSAS refinements from distinguishing between the two models. While the differentiation of the structural model is not definitive, the sample is shown to be phase pure by the absence of any impurity reflections. Parameters are fixed where no errors are given.
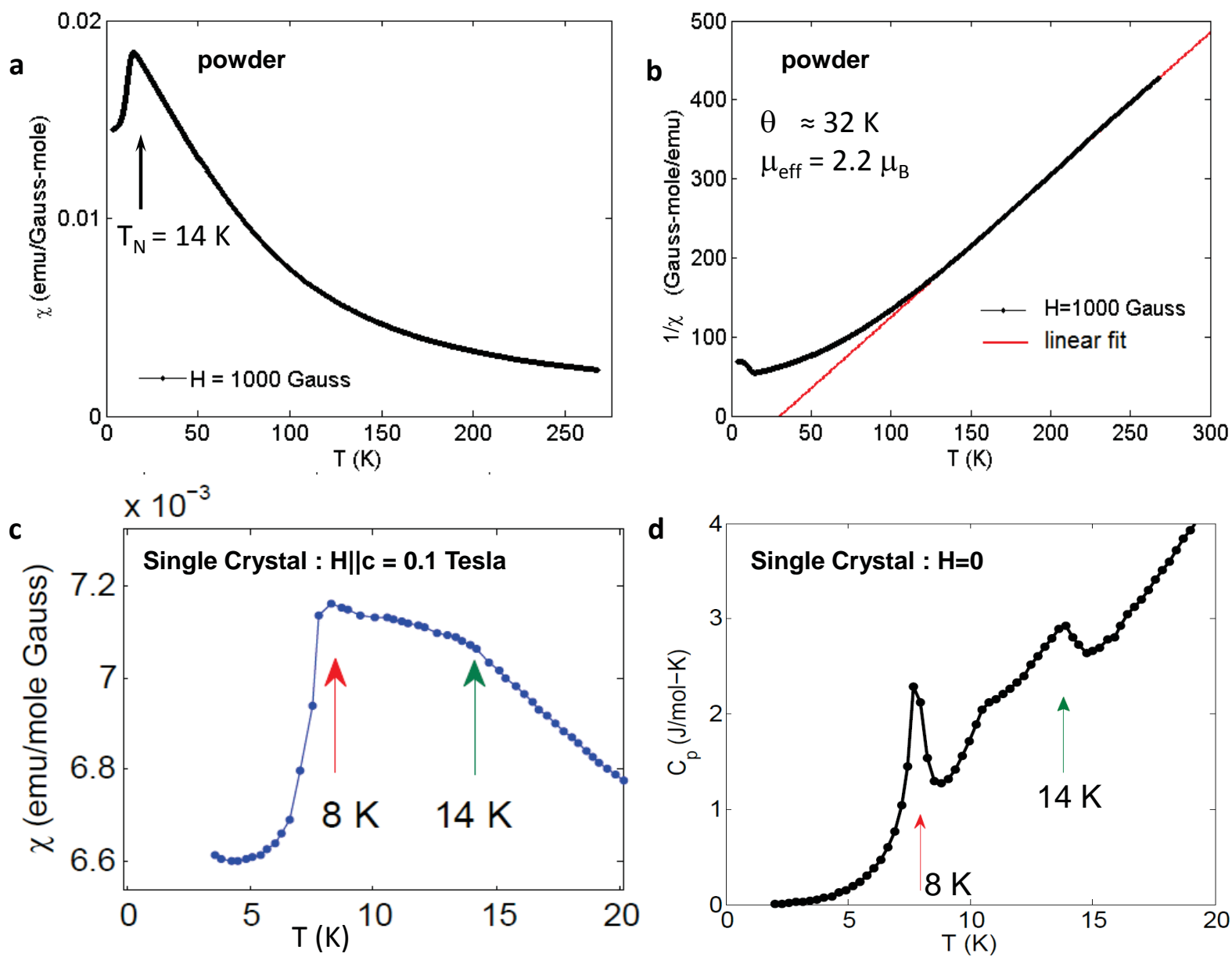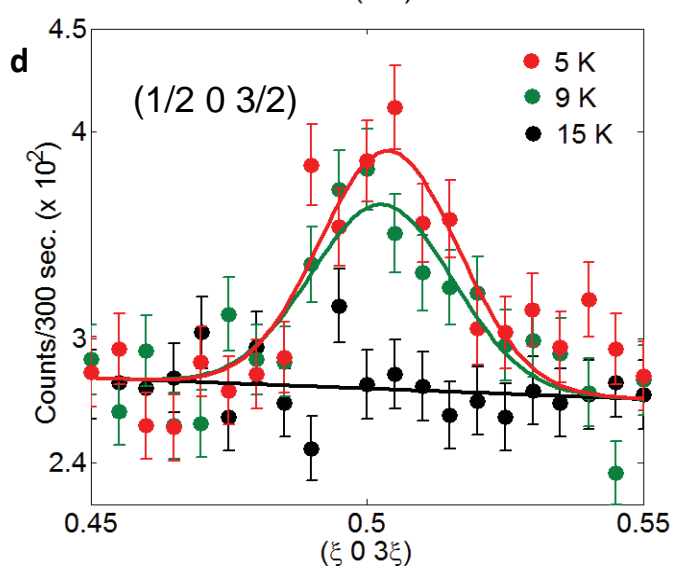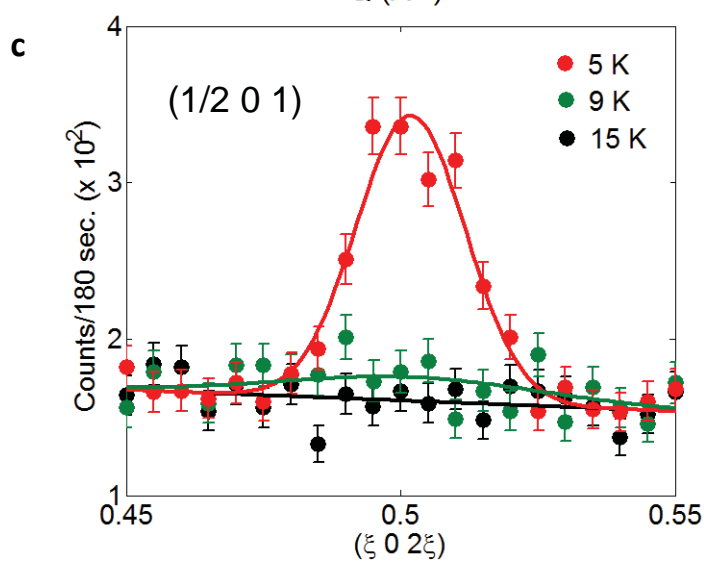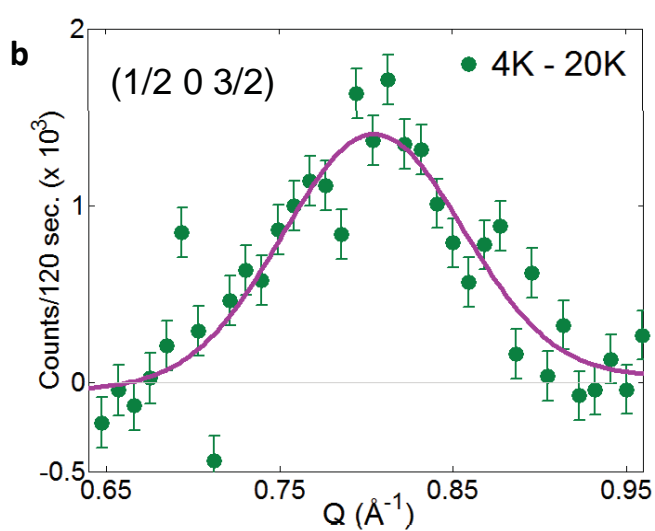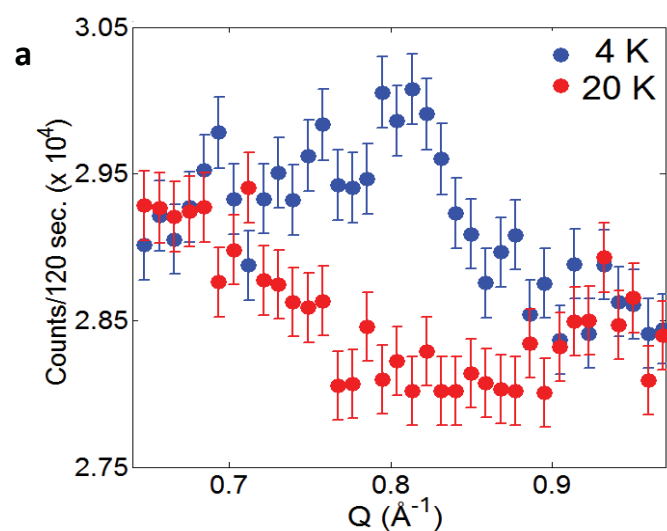
Supplementary Fig. 1

Supplementary Figure 1: The magnetic susceptibility and heat capacity of single-crystal and powder α-RuCl₃. a, The magnetic susceptibility χ for powder α-RuCl₃ showing only one anomaly at $T_N \approx 14$ K. **b,** The $1/\chi$ plotted versus temperature. The data between 100 and 273 K fits to a straight line which yields $\theta \approx 32$ K, and $\mu_{eff} \approx 2.2$ μ_B. **c-d,** The magnetic susceptibility with H∥c = 0.1 Tesla and the heat capacity with H=0 of the single-crystals of α-RuCl₃ are shown. Both shows at least two distinct anomalies - the 8 K (sharper, red arrow) and the 14 K (broader, green arrow) corresponding to Neel transitions of the (1/2, 0, 1) and (1/2, 0, 3/2) antiferromagnetic orders respectively, as shown in Fig. 1d,e in main text and Extended Data Fig. 3 below.

a

b

c
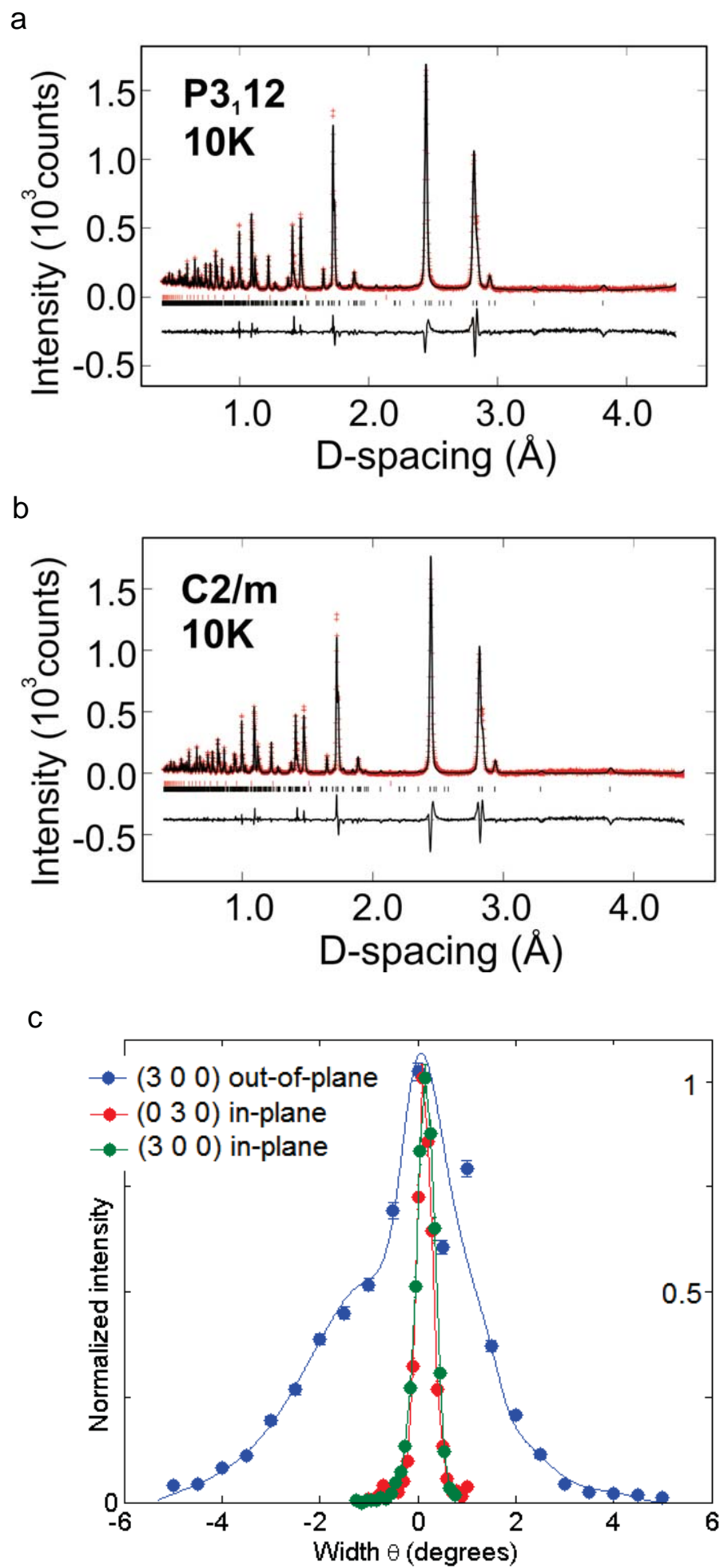
Supplementary Fig. 2

Supplementary Figure 2: Powder diffraction data and single-crystal rocking curves. a-b.
Powder neutron diffraction pattern obtained at the POWGEN beamline at SNS at 10 K. The Rietveld analysis of the data is performed using GSAS for both the $P3_1 12$ (a) and $C2/m$ (b) space groups. All the sample peaks are accounted for by the Rietveld analysis, which thus exhibit the phase purity of the powder sample. The fitted lattice parameters are in Supplementary Table 2. **c.**Neutron diffraction data on a single-crystal showing in-plane versus out-of-plane rocking curves for a (3 0 0) order Bragg peak. In-plane rocking scans are illustrated for two equivalent Bragg reflections, and in each case the in-plane mosaicity is resolution limited (FWHM~0.3°), proving a high degree of in-plane order. Conversely the out-of-plane mosaicity is broad (FWHM~4°) pointing to presence of structural disorder arising from stacking faults.

Supplementary Fig. 3

Supplementary Figure 3: **Magnetic Bragg peaks in α-RuCl$_3$.** **a,** Neutron diffraction raw data from 5.3 grams of powder sample at T = 4 K and 20 K revealing magnetic Bragg peak at Q $\approx$ 0.81 Å^{-1}. **b,** Point by point difference plot (4 K *minus* 20 K) of the data in **a**. The solid purple line shows a Gaussian fit revealing the magnetic Bragg peak at Q = 0.81(1) Å^{-1}. This corresponds to the (1/2 0 3/2) wave-vector. **c-d,** Radial scans on a 22.5 mg single-crystal of RuCl$_3$ through the (1/2 0 1) peak (**c**) and the (1/2 0 3/2) peak (**d**). Note that the (1/2 0 1) order vanishes by T = 9 K, unlike the (1/2 0 3/2) order. This confirms that the two magnetic orders with the same in-plane (1/2, 0), but different out of plane wave-vectors (L = 1 and 3/2) exist, and are responsible for the magnetic anomalies observed in the magnetic susceptibility and heat capacity.
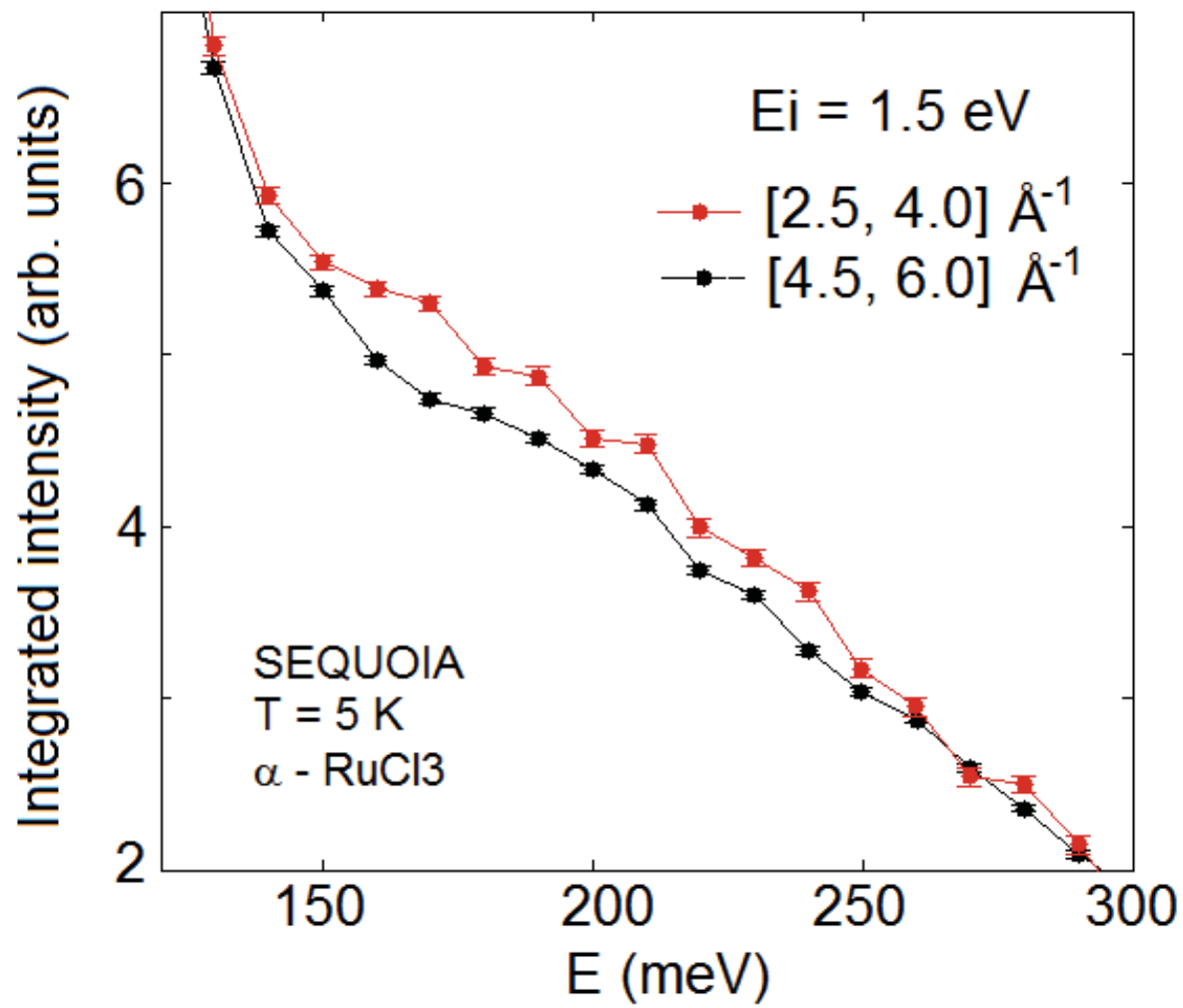
Supplementary Fig. 4

Supplementary Figure 4: **Raw data for E_i = 1.5 eV at two wave-vectors.** The constant Q cuts through the empty-can subtracted inelastic neutron powder data taken at SEQUOIA chopper spectrometer with E_i = 1.5 eV for two representative Q ranges one at low Q and the other at high Q as shown. The lower Q cut shows a higher intensity than the higher Q cut which represents magnetic scattering from the spin orbit coupling mediated $J_{1/2} \rightarrow J_{3/2}$ transition. The difference between these two cuts is the peak shown in Fig. 2a in main text.
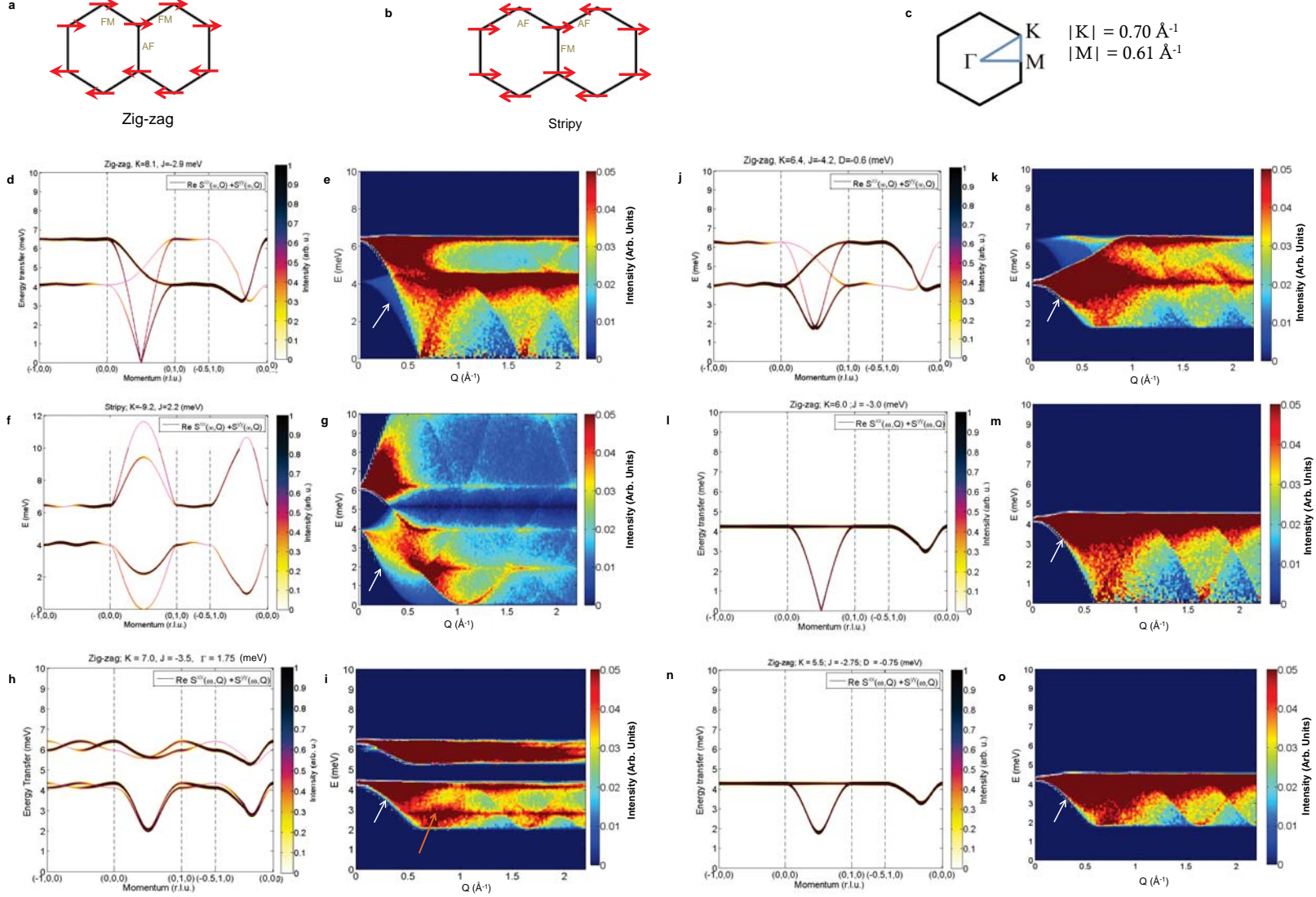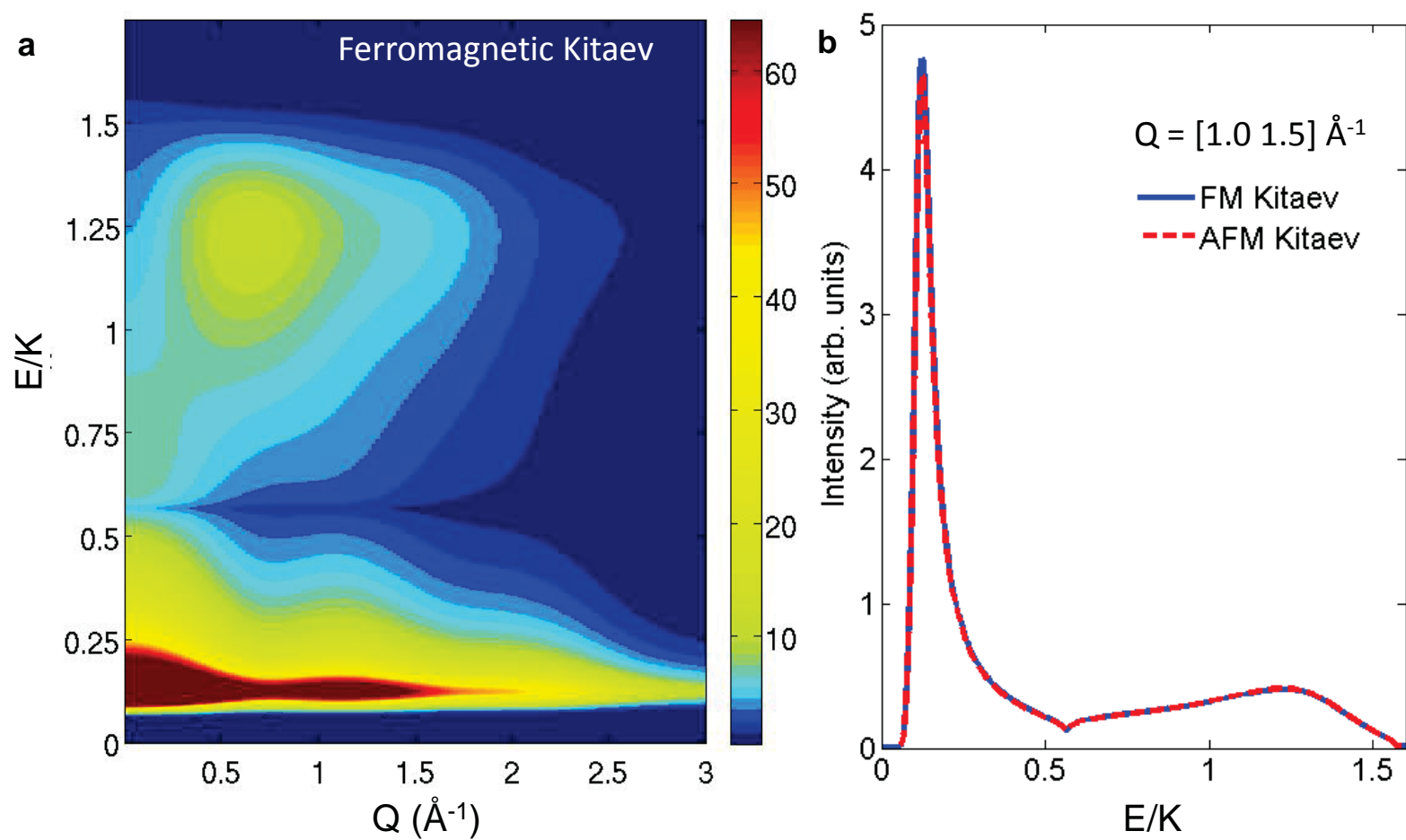
Supplementary Figure 5

**Supplementary Figure 5**: **Spin Wave Theory calculations and corresponding powder averages. a,** Zig-zag and **b,** stripy structures. For each spin two-thirds of the nearest neighbors are co-aligned in the zig-zag, and anti-aligned in the stripy magnetic structures. **c,** The nominal in-plane honeycomb reciprocal lattice. The values noted are for the room temperature lattice constants for α-RuCl$_3$. **d-e,** The SW spectrum for the parameters corresponding to $(K, J) = (8.1, -2.9)$ meV with a zig-zag ground state, and the corresponding powder averaged scattering cross-section yields intensity bands at 4 and 6.5 meV. We note that this solution corresponds to an alternate choice of ω_1 and ω_2 compared to that shown in Fig. 4 of the main text. This choice gives a much worse description of the observed intensity of the lower mode. **f-g,** The SW spectrum for a stripy ground state with parameters $(K, J) = (-9.4, 2.2)$ meV chosen to match the energies E_1 and E_2. The corresponding powder averaged pattern does not match the data in Fig. 3a. **h-i,** The SW spectrum for the J-K-Γ model[33-37] with parameters corresponding to $(K, J, \Gamma) = (7.8, -4.8, \pm1.45)$ meV with a zig-zag ground state and a gap of roughly 2 meV at the M point of the reciprocal lattice. Corresponding powder averaged pattern yields additional intensity bands (orange arrows) arising from broken band degeneracy not seen in our data in Fig. 3a. **j-k,** The spin wave spectrum for the H-K model plus an additional Ising term DS^zS^z, with parameters $(K, J, D) = (6.4, -4.2, -0.6)$ meV with a zig-zag ground state showing a gap of roughly 2 meV at the M point. Note that the anisotropic H-K model with parameter set $K^{\alpha\alpha} = K^{\beta\beta} = K^{\gamma\gamma}/1.1 = 6.4$ meV, and J = -4.2 meV also shows a similar gapped spectrum. **l-m** A solution with $K = -2J$ shows only one mode at the position of M_1, here illustrated with parameters $(K, J) = (6.0, -3.0)$ meV. **n-o** Adding an Ising term when $K=-2J$ introduces a gap but does not break the band degeneracy, shown here with $(K, J, D) = (5.5, -2.75, -0.75)$ meV leading to a gap of roughly 2 meV. In all cases, the scattering cross-section includes the single-ion Ru^{3+} form factor[46]. The

white arrows in the powder averaged spectra indicate the shapes of the edge of the lower modes. Experimental results shown in Fig. 3a are compatible with the zig-zag, but not the stripy, ground state. The chosen ranges of the reciprocal lattice plotted are the same as those in Ref. 38.

a Ferromagnetic Kitaev

b Q = [1.0 1.5] Å^{-1}
FM Kitaev
AFM Kitaev

Supplementary Fig. 6

Supplementary Figure 6: **Powder averaged simulations of the isotropic pure-Kitaev calculations following Ref. 10. a,** The powder averaged pattern with isotropic *ferromagnetic* Kitaev interactions. **b,** The constant Q cuts with Q = [1.0, 1.5] Å^{-1} for the antiferromagnetic and ferromagnetic Kitaev interactions show similar intensities for both the upper and the lower modes. The upper mode is broad in both cases.
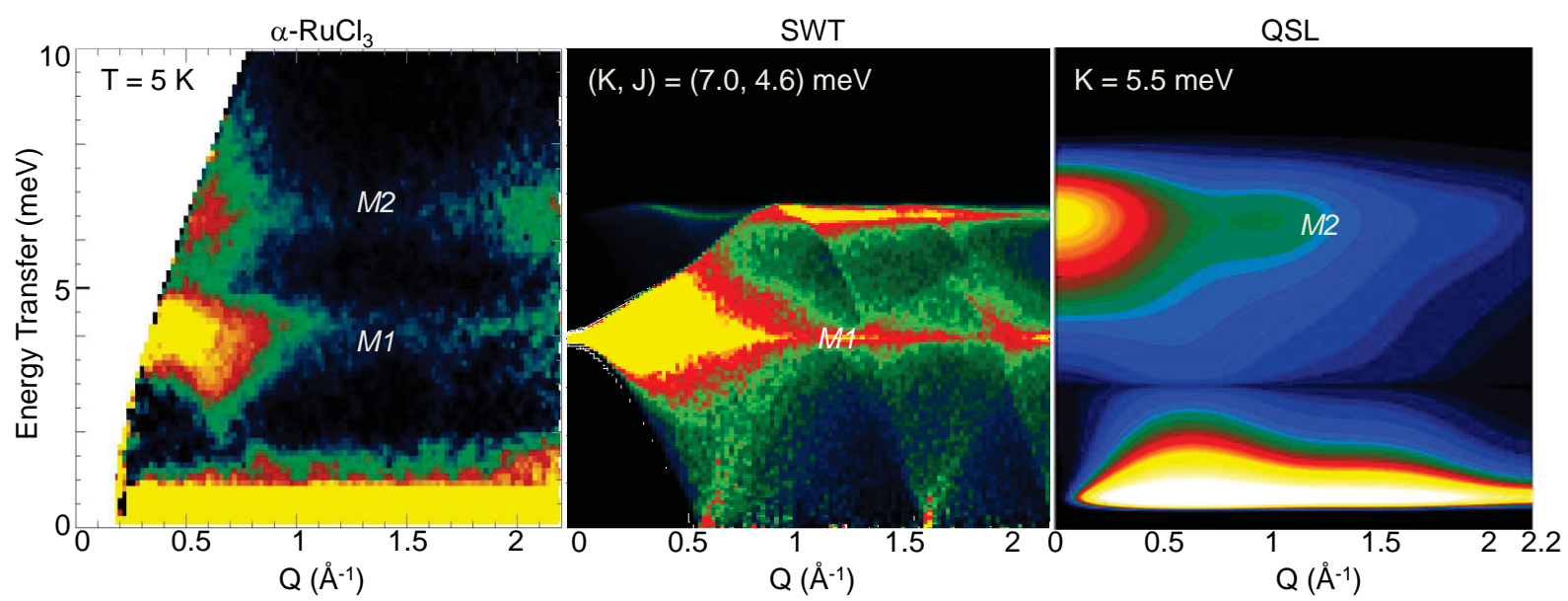
Supplementary Fig. 7

Supplementary Fig. 7. Visual synopsis of Q and E dependence of the scattering: We show the data obtained with $E_i = 25$ meV at $T = 5$ K (Fig. 3a) side-by-side with the SWT result (Fig. 4a) and pure Kitaev QSL predictions (Fig. 5d). The comparison provides a visual synopsis of the main result of this paper. We note that the energy width and wavevector dependence of the M_2 mode is inconsistent with the SWT calculation, but in fact is accounted for rather well by the Kitaev calculation. The solution set $(K, J) = (7.0, -4.6)$ meV is chosen for the SWT as these parameters give the best quantitative description of the lower mode within a SW calculation of the H-K model.

1   **Supplementary Information:**

2

3   **Susceptibility and Heat Capacity measurements:** See Supplementary Figure 1. The ratio of

4   the intensities for the $T_{N1} = 8$ K and $T_{N2} = 14$ K Neel transitions varies from crystal to crystal

5   depending on growth conditions. These have previously been suggested to be signatures of

6   different[27], or possibly exotic[25,29], phase transitions in the system. The present work shows that

7   they arise from domains with different stacking orders in a highly two-dimensional system. This

8   also naturally explains the sample to sample variation of the bulk measurements. The single-ion

9   effective moment is estimated (see Supplementary Fig. 1) to be 2.2 μ_B, which in susceptibility

10   measurements correspond to $\sqrt{J(J + 1)}g$, where g is the Lande g factor.

11

12   **Neutron Diffraction and Magnetic Bragg peaks:** Powder neutron diffraction data was

13   obtained at the POWGEN TOF neutron diffraction beamline at SNS in a standard sample-

14   changer fitted to a 10 K cryostat. Supplementary figures 2a and 2b show the data obtained at

15   Bank-2 of the beamline and their refinement using GSAS. The structural parameters at 10 K are

16   shown in Supplementary Table 2. The structure is found consistent with the polytypes $P3_1$

17    $12^{22,23,S1}$, as well as $C2/m^{S2}$ at low temperature, both showing comparable fit quality. Both

18   refinements contain the RuCl$_3$ phase and a vanadium phase to account for weak peaks from the

19   vanadium sample can. We observed that stacking faults affect most of the (H00) and (H01) type

20   peaks, which showed a saw-tooth like Warren line shape. GSAS powder refinement routines

21   cannot properly model the high degree of stacking faults present, and this introduces

1   uncontrolled systematic uncertainties into the detailed crystallographic parameters obtained from

2   the refinement. Nevertheless the data clearly indicate that the sample is pure. There are no

3   additional peaks that would indicate potential impurity phases, such as β-$RuCl_3$, $RuOCl_2$, Ru or

4   RuO_2. No obvious phase transition was observed between room-temperature and 10 K. For this

5   paper we adopt the $P3_1$ 12 nomenclature which has been proposed for this system and which we

6   find consistent with the data[S1]

7

8   Magnetic neutron diffraction was performed on both single-crystal and powder samples of α-

9    $RuCl_3$ at the HB-1A Fixed Incident Energy (E_i = 14.68 meV) beamline at the High Flux Isotope

10   Reactor (HFIR) at ORNL. Single-crystal rocking curves are shown in Supplementary Figure 2c.

11   Magnetic Bragg peaks are shown in Supplementary Figure 3. Powder diffraction showed one

12   clear magnetic peak at $Q \approx 0.81$ Å^{-1}, and its weak second harmonic at $2Q \approx 1.62$ Å^{-1}.

13   Supplementary Fig. 3b shows the magnetic Bragg peak which is fitted to a Gaussian to reveal the

14   exact location of the peak at $Q = 0.81 \pm 0.01$ Å^{-1}. This corresponds to either (1/3, 1/3, 1) with a

15   120° order, or (1/2 0 3/2) with a zig-zag or stripy order. To confirm this, the single-crystal

16   diffraction was performed using one single-domain 22.5 mg crystal under identical experimental

17   conditions to the powder diffraction. Supplementary Fig. 3c,d show the single-crystal magnetic

18   diffraction peaks and their temperature dependence. As shown, we see co-existent magnetic

19   peaks at two different wave-vectors, $\vec{k_1}$ = (ξ 0 2ξ) and $\vec{k_2}$ = (ξ 0 3ξ) where ξ=1/2, with two

20   different transition temperatures T_{N1} = 8 K and T_{N2} = 14 K, precisely matching the Neel

21   transition temperatures obtained from the heat capacity measurements in Fig. 1d and

22   Supplementary Fig. 1. A search yielded no evidence of peaks for 120° order at the (1/3, 1/3, L)

2

locations, which can hence be precluded. The ordered moment size is estimated by comparing

the structural Bragg peak intensities with the magnetic Bragg peaks, and yields a lower bound of

$0.20(5)$ μ_B that can be inferred by assuming that the moment direction is perpendicular to the

magnetic *k* vector. The moment direction is not completely resolved in our measurements,

however from the constraints imposed by measuring peaks in different directions an upper bound

can be ascertained for the total ordered moment, to be $0.4(1)$ μ_B. Thus the ordered moment is at

most around 35% of the value of the effective moment measured from susceptibility. Note that

the ordered moment size in neutron scattering measurements corresponds to $g\langle J^{\alpha}\rangle$, where *g* is

the Lande *g* factor and α corresponds to the direction of the ordered moment.

As discussed in the main text, the powder data does not show statistically significant

evidence for a peak at 0.7Å^{-1} corresponding to the $(1/2,0,1)$ position. If such a peak is included

in a fit it is present with an intensity of approximately 10% of that at the $(1/2,0,3/2)$ position

although the peaks are not well resolved. This is not surprising when considering the low energy

necessary to induce stacking faults and the ease of introducing them by mechanically working

the sample. If the neighboring layers of one fixed layer are assumed to be one of the other two

possibilities, but occurring with similar probabilities, the average length of an ABCABC ordered

domain extends over very few lattice spacings, and most of the sample will be composed of

ABAB type ordered regions. This is reflected in the presence of only a single observed

transition in the powder samples, which also simplifies the interpretation of the observed

inelastic scattering.

The Spin-Orbit coupling mode: In a simple picture the spin-orbit coupling leads to a dispersionless magnetic mode of energy $E = 3\lambda/2$ corresponding to the $J_{1/2} \rightarrow J_{3/2}$ transition. The neutron scattering cross-section for this mode varies as the square of the magnetic form factor of the Ru^{3+} ion and therefore decreases with increasing Q. This allows one to distinguish magnetic modes from other scattering processes. This is evident in the extra scattering at low Q visible in Supplementary Figure 4. The large background at high Q (shown in Figure 2b) arises from several sources including multi-phonon and multiple scattering. Over the region shown a Q independent background is a reasonable approximation.

Spin wave models for zig-zag ground states plus extended Hamiltonians: Spin wave calculations have been performed for both zig-zag and stripy ordered ground states which are illustrated in Supplementary Figure 5a,b with the Brillouin zone shown in 5c. As mentioned in main text, the spin wave minimum occurs at 0.6 Å^{-1}, corresponding to the M point of the 2D lattice, as opposed to the 3D wave ordering vector of 0.8 Å^{-1}. This is strong evidence that interplanar coupling of the spins is small, and a two dimensional analysis can describe most features of the relevant spin waves. These calculations are hence performed in a strictly two dimensional limit, and therefore do not capture details of the low energy spin waves that may be dependent on the precise stacking arrangement of the honeycomb lattices. The addition of interplanar coupling will result in some small dispersion of spin waves along the c* direction with a minimum at the 3D ordering wave-vector. As revealed in simulations including such a coupling, this also leads to observable singularities separated by the same energy scale. Such

1 features have not been observed in the highest resolution data taken with $E_i = 8$ meV, allowing

2 for an estimate of an upper bound for the interplanar magnetic coupling on the order of 0.3 meV.

3 We note that recent calculations suggest that the interlayer binding energy is of order only a few

4 micro-eV/unit-cell[S3], suggesting that effects on the 2D excitations arising from stacking faults

5 are likely to be negligible.

6

7 As discussed below, we have carried out numerous different simulations to investigate the

8 possible effect of additional Hamiltonian terms on the excitation spectrum and corresponding

9 powder averaged scattering.   The powder measurement averages over directions in Q, but

10 preserves singularities arising in the density of states as a function of E. The scattering cross-

11 sections can be readily calculated and it is seen that the powder neutron spectrum contains

12 distinctive fingerprints of the Hamiltonian which can be readily compared to theoretical

13 calculations to obtain approximate parameters. This is especially true if the measurements are

14 high resolution, allowing for the extraction of the intensities and widths of the features with high

15 accuracy. In our data, any extra modes will be well-resolved to the instrumental resolution of

16 ~0.5 meV (at 6 meV) which puts an absolute lower bound on the resolvability of the features.

17 Various combinations of all parameters known to us that have been suggested to describe the

18 system, including the Γ and Γ' terms, have been used for our spin wave simulations. We have

19 not found any of these that satisfactorily fit our powder averaged data.

20

21

1   For illustrative purposes we consider the Hamiltonian including the H-K terms as well as

2   the symmetry allowed off-diagonal exchange term, Γ[35]:

3

4    $$\mathcal{H} = \sum_{i,j}\left(KS_i^m S_j^m + J\vec{S_i} \cdot \vec{S_j} + \Gamma(S_i^m S_j^n + S_i^n S_j^m)\right).$$ …   eqn. (S1)

5

6   Representative calculations with different values of K, J and Γ, and additional Ising terms are

7   shown in panels d – o of Supplementary Figure 5. Supplementary Fig. 5 d,e shows the scattering

8   from the alternate set of parameters (K,J) inferred from the spin wave analysis discussed in the

9   main text. Supplementary Fig. 5 f,g illustrates the inelastic scattering expected for a stripy

10   ground state, which is seen to be completely incompatible with the data.

11

12   As discussed in the main text, the observed M_1 scattering has an energy gap $\Delta \geq 1.7 \pm 0.1$ meV

13   that is established by analyzing the $E_i = 8$ meV constant Q cut at the M point band minimum, Q

14   $= 0.62(3)$ Å^{-1}. With $\Gamma = 0$ the H-K SWT cannot reproduce the experimentally observed gap.   A

15   non-zero Γ term can induce a gap at the M point. However, it also lifts mode degeneracies, and

16   as described in main text, when it is large enough to match the experimental gap value it also

17   yields additional singularities in the powder averaged spectrum that are not seen experimentally.

18   To assess whether or not spin wave theory can explain the broad energy response of the M_2

19   mode, a numerical search of $(K$-J-$\Gamma)$ parameter space was conducted.   Supplementary Figure

20   5h,i shows one of the best solutions found with parameter set $[K, J, \Gamma] = [7.0, -3.5, \pm 1.75]$ meV.

21   This solution produces an unbroken band of scattering at M_2 with about half of the observed

1   width, but is contradicted by the data as it predicts extra singularities in the lower mode (orange

2   arrow) that are not observed. A smaller Γ does not broaden the upper mode appreciably to match

3   the data, while a larger Γ both splits the M_2 band and makes the unobserved additional mode in

4   M_1 much more prominent. The addition of arbitrary extra Heisenberg terms (such as next-

5   nearest neighbor terms) to equation 1 to artificially broaden the upper mode also breaks the

6   degeneracy of the modes creating extra singularities and at lower energies not observed in the

7   data.   As argued in the main text, the line-shape of the M_2 mode cannot be satisfactorily

8   accounted for by adding extra modes or bending the bands.

9

10   We also note that an additional Ising-like anisotropy, which includes anisotropic Kitaev

11 terms as a special case, also leads to a gap in SWT without creating any extra bands:

12

13 $$\mathcal{H} = \sum_{i,j}\left(K S_i^m S_j^m + J\vec{S_i}\cdot\vec{S_j} + D_\rho S_i^\rho S_j^\rho\right).$$ …   eqn. (S2)

14

15 Supplementary Fig. 5j,k shows a calculation for the special case $\rho = z$, chosen to match the

16 experimental gap.   Notably, this scenario is equivalent to introducing anisotropy in the Kitaev

17 term of the H-K model with one of the three components increased by roughly 10% relative to

18 the other two components, in the two solutions marked in Fig. 4(d) inset. Although there is no

19 physical motivation for the assumption of an Ising-like term in the Hamiltonian, one cannot

20 absolutely rule out the possibility of an anisotropy in the Kitaev terms. However, the calculated

21 spin wave scattering does not reproduce the energy width of the M_2 mode.   We note that it has

1   been suggested that the Hamiltonian for α-RuCl$_3$ should be XY like as opposed to Ising-like[29].

2   SWT calculations with an XY anisotropy are not compatible with the inelastic neutron scattering

3   data.

4

5   Note that all of the SW simulations illustrated above assume the presence of long-range order,

6   and hence none of them can explain the experimental temperature dependence of the M$_2$ mode

7   (Fig. 5b) which extends well beyond the ordering temperature.

8

9   As an interesting aside, the ratio K/J =-2 has been suggested previously for interactions in

10 trigonally symmetric lattices with magnetic cations interacting via three edge-shared octahedral

11 anions. (see, e.g., equation 5.8 in Ref. S4). With this ratio the SWT has additional degeneracies,

12 and the result is the appearance of only the M$_1$ mode, as depicted in Supplementary Fig. 5l-m

13 and also in Supplementary Fig. 5n-o with an additional Ising term leading to a gap. The possible

14 relevance of this is discussed further below.

15

16 **Wave-vector dependence of the intensity above T$_N$:** In typical antiferromagnets above the

17 ordering temperature T$_N$ the system is in a disordered state with short range order characterized

18 by a correlation length ξ. Under this circumstance propagating spin waves can still appear at

19 reduced wave-vectors q such that $q\xi \gtrsim 1$, i.e. close to an antiferromagnetic zone boundary. If an

20 apparently well-defined peak arises from the zone boundary scattering, a constant E scan in a

21 powder can exhibit structure when Q has a magnitude equal to that of the zone boundary in any

22 magnetic Brillouin zone.   Moreover, the powder averaged measurement for a quasi-2D system

includes contributions from all 2D zone boundaries with $Q^{2D}_{ZB} \leq Q$. Thus, the monotonic decrease intensity as a function of Q observed for M_2 is unexpected for SWT, however it matches the calculated scattering from the Kitaev QSL.

Pure Kitaev Model: With the validity of the spin-waves in question because of the low ordered moment, and given the continuity of the high-energy mode across the Neel transition, we argue that the pure Kitaev model is a more appropriate description of the physics for the higher energy mode. Calculations for the both antiferromagnetic and ferromagnetic pure Kitaev interactions[10] (i.e. with no Heisenberg contributions) are shown to also produce two modes in the powder average as is shown in Fig. 5d and Supplementary Fig. 6. For both cases, the intensity originates from Majorana fermions in the presence of a heavy Z_2 flux pair. In particular, in the limit of vanishing Heisenberg interactions, the lower mode originates from Majorana Fermions strongly affected by the pair of fluxes. The upper mode at a scale $E \sim K$ originates from high energy Majorana fermions which are much less sensitive to the local scattering by the flux pair, or the magnetic LRO; this mode therefore more closely resembles the Majorana density of states in this energy region. As discussed in the main text the response is broad in both energy and momentum, and can here be directly related to the broadness of the Majorana Fermion DOS in the presence of a flux pair. The broad M_2 mode from deconfined Majorana Fermions is insensitive to energy scales of the interlayer coupling. Our results in $RuCl_3$ hence place this material as a particularly strong contender for further studies of the properties of 2D Majorana physics.

1   While we have carried out two parallel analyses (classical SWT and QSL) describing the

2   location and behavior of both modes, both ultimately derive from the same microscopic

3   Hamiltonian. The full description of the magnetic response function at all energies and

4   temperatures will thus require a complete quantum theory of the excitations of the Heisenberg-

5   Kitaev Hamiltonian, possibly with additional terms. Such a treatment is not available with

6   present technology. In absence of the above all-inclusive quantum H-K theory, one ansatz

7   popular in the literature attempts to treat both the modes together in SWT using the H-K

8   Hamiltonian. This generally permits an approximate evaluation of interaction parameters. For

9   systems that show magnetic order, where SWT is appropriate as a low-energy theory, the

10 interaction parameters derived in this fashion can often be employed to infer the nature of the

11 ordered ground states .

12

13 **Comparison of wave-vector dependence of the Kitaev and spin-wave models:** For

14 convenience of comparison, the supplementary Figure 7 shows a direct comparison of the low

15 temperature response function of α-RuCl$_3$ (Fig. 3a), spin-wave theory (Fig. 4b), and the pure

16 Kitaev calculation (Fig. 5d).

17

18 **An alternate single-mode scenario:**

19 One can check for robustness of the fitted value of K from SWT by treating an alternate

20 hypothetical scenario where the spin wave spectrum is fitted to optimally reproduce only the

single lower mode M_1, leaving the origin of the upper mode M_2 a priori undetermined. As discussed above, this can be done by choosing $K=-2J$ where ω_1 and ω_2 coincide. With this choice $K = 6$ meV yields only one band of intensity corresponding to the location of M_1 at 4.2 meV. Supplementary fig. 5 l-m shows the calculation and their powder average for the gapless case, while Supplementary fig. 5 n-o with parameters $K = -2J = 5.5$ meV, D = -0.75 meV (or alternatively, $K^{\alpha\alpha} = K^{\beta\beta} = K^{\gamma\gamma}/1.14 = -2J = 5.5$ meV) represents the gapped scenario. As we see, this ansatz yields values and sign of K and J values in the vicinity of the two solutions obtained above and hence the listed parameters remain valid even in this scenario. Crucially, $K = 6$ meV continues to reproduce the location of the M_2 mode at E ≈ 6 meV in our Kitaev-only QSL computation.

References for Supplementary

S1. Stroganov, E.V. and Ovchinnikov, K.V., *Vestitik Leningrad Lrniv., Sev. Fix. i Khim.,* **152** (1957).

S2. Brodersen, K., Thiele, G., Ohnsorge, H., Recke, I., and Moers, F., *Journal of the Less Common Metals* **15**, 347 (1968).

S3. Kim, H-S. and H-Y Kee, H-Y, Structural properties of α-RuCl$_3$: an *ab-initio* study, arXiv:1509.04723 (2015).

S4. Khaliullin, G., Orbital Order and Fluctuations in Mott Insulators. *Prog. Theo. Phys. Suppl.* 7, **160**, 155 (2005).